

From NaZn_4Sb_3 to $HT\text{-Na}_{1-x}\text{Zn}_{4-y}\text{Sb}_3$: Panoramic Hydride Synthesis, Structural Diversity, and Thermoelectric Properties

Volodymyr Gvozdetskyi,[†] Bryan Owens-Baird,^{†,‡,§} Sangki Hong,[†] Tori Cox,[†] Gourab Bhaskar,[†] Colin Harmer,^{†,‡} Yang Sun,[‡] Feng Zhang,[‡] Cai-Zhuang Wang,^{‡,§} Kai-Ming Ho,^{‡,§} and Julia V. Zaikina^{*,†,§}

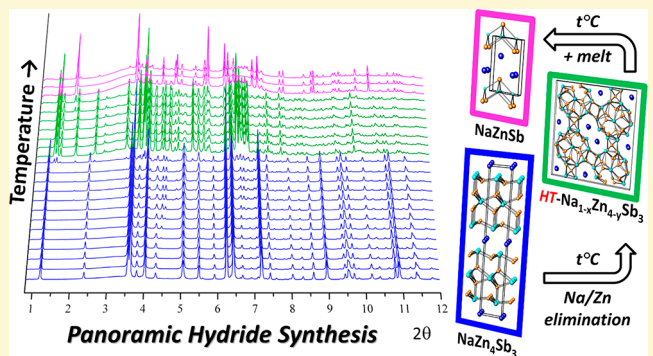
[†]Department of Chemistry, Iowa State University, Ames, Iowa 50011, United States

[‡]Ames Laboratory, U.S. Department of Energy, Ames, Iowa 50011, United States

[§]Department of Physics & Astronomy, Iowa State University, Ames, Iowa 50011, United States

Supporting Information

ABSTRACT: Two new sodium zinc antimonides NaZn_4Sb_3 and $HT\text{-Na}_{1-x}\text{Zn}_{4-y}\text{Sb}_3$ were synthesized by using reactive sodium hydride, NaH , as a precursor. The hydride route provides uniform mixing and comprehensive control over the composition, facilitating fast reactions and high-purity samples, whereas traditional synthesis using sodium metal results in inhomogeneous samples with a significant fraction of the more stable NaZnSb compound. NaZn_4Sb_3 crystallizes in the hexagonal $P6_3/mmc$ space group (No. 194, $Z = 2$, $a = 4.43579(4)$ Å, $c = 23.41553(9)$ Å) and is stable upon heating in vacuum up to 736 K. The layered crystal structure of NaZn_4Sb_3 is related to the structure of the well-studied thermoelectric antimonides $Ae\text{Zn}_2\text{Sb}_2$ ($Ae = \text{Ca}, \text{Sr}, \text{Eu}$). Upon heating in vacuum, NaZn_4Sb_3 transforms to $HT\text{-Na}_{1-x}\text{Zn}_{4-y}\text{Sb}_3$ ($x = 0.047(3)$, $y = 0.135(1)$) due to partial Na/Zn evaporation/elimination, as was determined from high-temperature in situ synchrotron powder X-ray diffraction. $HT\text{-Na}_{1-x}\text{Zn}_{4-y}\text{Sb}_3$ has a complex monoclinic structure with considerable degrees of structural disorder ($P2_1/c$ (No. 14), $Z = 32$, $a = 19.5366(7)$ Å, $b = 14.7410(5)$ Å, $c = 20.7808(7)$ Å, $\beta = 90.317(2)^\circ$) and is stable exclusively in a narrow temperature range of 736–885 K. Further heating of $HT\text{-Na}_{1-x}\text{Zn}_{4-y}\text{Sb}_3$ leads to a reversible transformation to NaZnSb above 883 K. Both compounds exhibit similarly low thermal conductivity at room temperature ($0.9 \text{ W m}^{-1} \text{ K}^{-1}$) and positive Seebeck coefficients ($38\text{--}52 \mu\text{V/K}$) indicative of holes as the main charge carriers. However, resistivities of the two phases differ by 2 orders of magnitude.



INTRODUCTION

Preparation of compounds, especially new phases, is oftentimes a bottleneck in the material discovery process. Computational predictions regarding stability, structures, and properties of novel compounds are proposed to guide experimentalists, but in order to accelerate materials discovery they should be verified by the targeted synthesis of new compounds.^{1–7} The vast number of synthesis parameters (e.g., temperature, pressure, composition, annealing time, cooling/heating rates), as well as kinetic limitations, make unguided solid-state synthesis serendipitous. In addition to the compositional space, the synthesis temperature is a decisive factor in the stabilization of a particular compound. In recent years, the advances in in situ X-ray and neutron diffraction and in situ TEM methods for reaction monitoring allow a better understanding of the mechanisms in solid-state reactions.^{3,8–17} For instance, high-temperature X-ray diffraction data of the $\text{Cs}/\text{Sn}/\text{P}/\text{Se}$ systems gave a “panoramic” view of the compositional phase space and allowed for the discovery of multiple new phases.³ Unprecedented photon density and high

resolution of synchrotron experiments have yielded high-quality data in a short time frame, which allows for precise study of relationships among phases upon heating or cooling within a very narrow temperature gradient. Using such methods, a “blind” synthetic pathway becomes clear and high-temperature intermediates detected from high-temperature X-ray diffraction can be further prepared ex situ.

The hydride synthetic route, which uses mixable salt-like hydride precursors (e.g., alkali metal hydrides AH , $A = \text{Li}, \text{Na}, \text{K}$), instead of ductile alkali metals, was successfully utilized for the synthesis of binary and ternary borides,^{7,18,19} antimonides,^{20,21} arsenides,^{22,23} silicides,^{24–27} and germanides.^{24,28} This method is particularly applicable for the compositional screening in the discovery of new ternary alkali zinc antimonides, providing composition control and high purity samples.²⁰ Traditional solid state synthesis using alkali metal

Received: June 10, 2019

Revised: October 1, 2019

Published: October 3, 2019

precursors is hampered by their ductility, high reactivity, and vapor pressure at elevated temperatures, as well as side reactions with crucible materials. Ductility of alkali metals prevents the intimate mixing of precursors, which oftentimes results in the inhomogeneous samples and impedes compositional control.

Interest in ternary Zintl phase antimonides^{29–33} stems primarily from the promising thermoelectric properties of some of the members of this vast family of the compounds, such as $Ae\text{Zn}_2\text{Sb}_2$ ($Ae = \text{Ca}, \text{Sr}, \text{Ba}, \text{Eu}$, or Yb)^{34,35} and $\text{Yb}_{14}\text{MnSb}_{11}$.^{36,37} Structural and compositional diversity of ternary antimonides containing transition or post-transition metals together with electropositive cations suggests that there are a number of undiscovered related phases with potentially enhanced properties. The hydride synthesis route allows for fast screening of compositional space for different systems at a chosen synthetic temperature. On the other hand, metastable intermediates or phases, which are stable only in a narrow temperature range, could be hidden.

Here, we have explored the ternary Na-Zn-Sb system and discovered two new compositionally similar but structurally different ternary antimonides, and both feature new structure types. Using the fast hydride route coupled with *in situ* high-temperature powder X-ray diffraction experiments, compositional and temperature screening allowed for synthesis of two new ternary phases: the NaZn_4Sb_3 phase and what at first appeared to be its polymorph, but in fact it is a different compound with slightly Na/Zn depleted composition $HT\text{-Na}_{1-x}\text{Zn}_{4-y}\text{Sb}_3$, stable in a narrow temperature range. The hydride route yields single phase samples of both antimonides, allowing for the experimental access to their transport properties. The crystal structures, synthesis, structural transformations, and transport properties of the NaZn_4Sb_3 and $HT\text{-Na}_{1-x}\text{Zn}_{4-y}\text{Sb}_3$ are discussed herein.

EXPERIMENTAL SECTION

Synthesis. Starting materials for synthesis were used as received: sodium hydride (Sigma-Aldrich, 95%), sodium metal (Alfa Aesar, 99.95%), zinc powder (Alfa Aesar, 99.996%), and antimony lump (Alfa Aesar, 99.9999%). All manipulations of reagents and samples were carried out under an inert argon atmosphere ($p(\text{O}_2) < 1 \text{ ppm}$, $p(\text{H}_2\text{O}) < 1 \text{ ppm}$) in a glovebox.

Hydride Route. Fine antimony powders were prepared beforehand by ball-milling antimony lumps for 12 min in ambient atmosphere using a standard grinding set with tungsten carbide inserts and high-energy ball-mill SPEX 8000 M MIXER/MILL. Afterward, powders of the sodium hydride, zinc, and antimony were weighted in a 1.03:4:3 molar ratio ($m = 0.7 \text{ g}$) and loaded into a polycarbonate grinding set with a methacrylate grinding ball. The vial was further sealed into two plastic bags under argon atmosphere and removed from the glovebox for ball-milling. Samples were ball-milled for 12 min to achieve sufficient mixing, while longer ball-milling caused partial decomposition of NaH . Inside the glovebox, freshly prepared fine powders were loaded into tantalum containers, which were sealed shut by arc-welding. The sealed tantalum ampules were removed from the glovebox and placed into silica reactors equipped with Swagelok safety check valves to prevent overpressurizing of the reactors due to hydrogen gas release during the heat treatment. The silica reactors were evacuated to $4 \times 10^{-5} \text{ bar}$ and placed into a resistance furnace (Thermo Scientific Thermolyne Type FD1500M) equipped with a temperature controller (Eurotherm 3216). Samples were slowly (1.4 K/min) heated from room temperature to 723 K, held at that temperature for 8 h, and cooled to room temperature naturally by switching off the furnace. A phase-pure NaZn_4Sb_3 compound can be prepared by following the synthetic method described above. Quenching samples with a Na:Zn:Sb molar ratio of 1.03:4:3 in

tantalum containers from higher temperatures (800 K) did not allow the stabilization of $HT\text{-Na}_{1-x}\text{Zn}_{4-y}\text{Sb}_3$. For synthesis of the $HT\text{-Na}_{1-x}\text{Zn}_{4-y}\text{Sb}_3$ phase, powders of the NaZn_4Sb_3 phase were loaded into graphitized silica tubes (5 mm diameter, 7 cm length), evacuated to $4 \times 10^{-5} \text{ bar}$, flame-sealed, rapidly heated from room temperature to 800 K (8.4 K/min), held there for 30 min (allowing for partial Na/Zn elimination), and quenched into cold water. Alternatively, the $HT\text{-Na}_{1-x}\text{Zn}_{4-y}\text{Sb}_3$ phase can be prepared using the hydride route in tantalum containers, with a Na and Zn depleted (~10%) composition, i.e., a NaH:Zn:Sb molar ratio of 0.93:3.61:3. Samples were slowly (1.7 K/min) heated from room temperature to 800 K, held at that temperature for 8 h, and quenched into cold water. Both compounds are air- and moisture-stable but were stored in a glovebox for further manipulations.

Synthesis from Elements: Single Crystal Growth. To obtain crystals suitable for single crystal X-ray diffraction, synthesis from elements and the heating profile with a slow cooling step was employed. A molar ratio of $\text{Na:Zn:Sb} = 1.7:4.7:3$ with a considerable excess of both Na and Zn was utilized, since samples with compositions closer to stoichiometric 1:4:3 molar ratio always contained a considerable amount of NaZnSb and binary zinc antimonides as impurities. For single crystal growth of the NaZn_4Sb_3 compound, elemental Na , Zn , and Sb were loaded into a graphitized silica tube, flame-sealed under vacuum, and heated from room temperature to 923 K (2.1 K/min), held at that temperature for 24 h, cooled to 473 K at a rate of 0.04 K/min, and cooled to room temperature by switching the furnace off. The same molar ratio 1.7:4.7:3 was utilized for single crystal growth of the HT -phase. The mixture was heated from room temperature to 873 K (2.4 K/min), held at that temperature for 12 h, cooled to 800 K at a rate of 0.015 K/min, and rapidly quenched in cold water. Single crystals of the NaZn_4Sb_3 or $HT\text{-Na}_{1-x}\text{Zn}_{4-y}\text{Sb}_3$ compounds were mechanically separated from the powders of NaZnSb , and additionally traces of binary zinc antimonides were present as impurities within the samples.

Characterization. Laboratory Powder X-ray Diffraction (PXRD). The purity of polycrystalline samples was checked by means of Rigaku MiniFlex600 powder diffractometer with $\text{Cu K}\alpha$ radiation ($\lambda = 1.540593 \text{ \AA}$) and a $\text{Ni K}\beta$ filter. Data were collected on a zero-background plate holder in air at room temperature. Phase analysis was performed using the PDF-2 database incorporated into PDXL program software.³⁸

Single-Crystal X-ray Diffraction (SC-XRD). Single crystal data were collected by means of Bruker D8 VENTURE diffractometer (Photon CMOS detector, Mo– $I\mu\text{S}$ microsource and Oxford Cryosystem 800 low temperature device) at 100 K for crystals of NaZn_4Sb_3 and $HT\text{-Na}_{1-x}\text{Zn}_{4-y}\text{Sb}_3$ (Tables 1 and 2). Data integration, absorption correction, and unit cell determination was performed by APEX 3 software.³⁹ The starting atomic parameters were obtained by direct methods with the SHELXS-2017.⁴⁰ Subsequently, the structures were refined using SHELXL-2017⁴⁰ (full-matrix least-squares on F_{o}^2).

NaZn_4Sb_3 . Crystals of the NaZn_4Sb_3 phase were found to be extensively twinned and/or weakly diffracting, hardly suitable for SC-XRD. Only basic crystallographic parameters, i.e., syngony, cell dimensions, and tentative structural model, though with reasonable interatomic distances, were extracted from experimental single crystal X-ray diffraction data. Due to weak intensity of reflections and insufficient crystal quality, the tentative structure solution was obtained first in triclinic syngony (space group $P\bar{1}$). The further symmetry analysis of atomic coordinates model using the Platon software package (command ADDSYM)⁴¹ indicates that the actual symmetry of the structure is hexagonal, space group $P6_3/mmc$ (No. 194), $Z = 2$, $a = 4.43579(4) \text{ \AA}$, $c = 23.41553(9) \text{ \AA}$, and $V = 399.003(5) \text{ \AA}^3$. This structural model was further used for Rietveld refinement from high-resolution synchrotron powder X-ray diffraction data (Table S1, Figure S1, Table 2).

$HT\text{-Na}_{1-x}\text{Zn}_{4-y}\text{Sb}_3$. Crystals of the $HT\text{-Na}_{1-x}\text{Zn}_{4-y}\text{Sb}_3$ phase were considerably larger and stronger diffracting than those of NaZn_4Sb_3 . Analysis of the diffraction data revealed pseudo-orthorhombic symmetry, e.g., monoclinic Laue symmetry with the β angle close

Table 1. Experimental Details and Crystallographic Data for the HT-Na_{1-x}Zn_{4-y}Sb₃ (Single Crystal X-ray Diffraction Data, 100 K)^a

refined composition	Na _{0.953(3)} Zn _{3.865(1)} Sb ₃
space group, <i>Z</i>	P2 ₁ /c, 32
cell parameters	
<i>a</i> , Å	19.508(3)
<i>b</i> , Å	14.708(3)
<i>c</i> , Å	20.736(4)
β , deg	90.402(5)
<i>V</i> , Å ³	5950(1)
temperature, K	100(2)
density g/cm ³	5.71
wavelength, Å	0.71073 (Mo K α)
absorption coeff., mm ⁻¹	22.92
min/max transmission	0.039/0.091
θ_{\max} deg	28.75
scan mode	continuous
crystal size, mm	0.4 × 0.3 × 0.2
measured reflections	104502
independent reflections	15401 ($R_{\text{int}} = 0.025$)
reflections with $F > 2\sigma(F)$	13212 ($R_{\sigma} = 0.038$)
parameters	602
GOF for F^2	1.13
final <i>R</i> -indices [$F > 2\sigma(F)$]	$R_1 = 0.039$, $wR_2 = 0.086$
<i>R</i> -indices (all data)	$R_1 = 0.050$, $wR_2 = 0.091$
larg. diff. peak and hole, e/Å ³	2.99/−1.75
structure solution	direct methods, SHELXS
structure refinement	least-squares, SHELXL

^aFurther details of the crystal structure refinement can be obtained from the Fachinformationszentrum Karlsruhe, 76344 Eggenstein-Leopoldshafen, Germany (fax: (+49)7247-808-666; e-mail: crysdata@fiz-karlsruhe.de) on quoting the depository number CSD 1919785.

to 90°, space group P2₁/c (No. 14). The positions of antimony and zinc atoms were obtained from direct methods (SHELXS).⁴⁰ Positions of sodium atoms were located from a combination of least-squares refinement and difference Fourier maps (SHELXL).⁴⁰ While in the determined model the interatomic distances were found to be within the reasonable range, the refinement has $R_1 \sim 6.5\%$, large inexplicable electron density peaks at the difference Fourier map, and deviation of the *E*-value statistics from 0.97 and 0.74 for ideal centric and acentric distributions (indicative of possible twinning). The data set was analyzed by COSET⁴² to determine the twin law, corresponding to the 2-fold rotation around the *a*-axis. Further refinement using commands TWIN (1 0 0 0 −1 0 0 0 −1) and BASF in SHELXL allowed R_1 values to be further reduced down to ~4%, while twin fraction was refined to ~7%. Further refinement revealed electron density peaks at the difference Fourier map located in a close proximity to the selected Zn or Sb atomic sites, and thus the split site model was considered. In this model the sum of site occupancy factors (s.o.f.) for an atomic site and its split counterparts was constrained to 100%, while the atomic displacement parameters (ADPs) were constrained to be the same: Sb(17)–Sb(25), Sb(21)–Sb(26), Sb(24)–Sb(27), Zn(16)–Zn(32), Zn(20)–Zn(33), Zn(27)–Zn(34), Zn(29)–Zn(35), Zn(30)–Zn(36), and Zn(31)–Zn(37) (Table S2). The refined s.o.f. for split Sb and Zn sites did not exceed 13% and 19%, respectively. Further refinement indicated that atomic displacement parameters (ADPs) for Na(5) and Na(8) sites were unambiguously larger comparing to the six other Na sites, thus, s.o.f. for Na(5) and Na(8) sites was refined and found to have partial occupancy of 84% and 75% respectively. Additionally, Zn(17) and Zn(23) atoms were found to be partially occupied (96.6% and 93.5%). More detailed analysis indicates complex crystallographic disorder that was modeled with series of constrains. For instance,

independently refined occupancies of Sb(17), Zn(20), and Zn(17) were found to be the same within 3 esd (estimated standard deviation). Therefore, the final refinement of the occupancies was done with the following constrains: either Sb(17), Zn(20), and Zn(17) atoms (refined s.o.f. 95.5%) or Sb(25) and Zn(33) atoms (refined s.o.f. of 4.5%) are present. Similar constrains were used for occupancies of Sb(21) and Zn(23) and Sb(24) and Zn(30). In the same manner, occupancies of Na(5) and Zn(31), Na(8), and Zn(16) and Zn(27) were constrained to be the same.

Further refinement indicates that atomic displacement parameters (ADPs) for Na(5) and Na(8) sites were unambiguously larger comparing to the six other Na sites, thus, s.o.f. for Na(5) and Na(8) sites was refined and found to have partial occupancy of 81% in both cases. Details of the data collection and refinement are summarized in Table 1, atomic coordinates, s.o.f., and ADPs are given in Table S2, and interatomic distances are listed in Table S3.

Synchrotron Powder X-ray Diffraction. High-resolution synchrotron powder diffraction data were collected at beamline 11-BM Advanced Photon Source (APS), Argonne National Laboratory (ANL), with an average wavelength $\lambda = 0.412804$ Å. Data were collected at room temperature and ambient pressure in a Kapton capillary.

High-temperature synchrotron powder X-ray diffraction data (HT-PXRD) was collected at beamline 17-BM (APS ANL) with an average wavelength $\lambda = 0.24130$ Å. Powdered samples of NaZn₄Sb₃ and HT-Na_{1-x}Zn_{4-y}Sb₃ were filled in a 0.7 mm outer diameter thick wall (0.1 mm) silica capillary and sealed under vacuum. The capillary was mounted into a secondary shield capillary (0.9 mm inner diameter, 1.1 mm outer diameter) located on a sample stage equipped with two resistive microheaters and a thermocouple set as close as possible to the measurement area. The further details of experimental setup can be found elsewhere.⁴³ Data were collected upon heating and cooling in the temperature range 298 K → 900 K → 298 K with a heating and cooling rate of 10 K min⁻¹ and 15 K min⁻¹ for NaZn₄Sb₃ and HT-Na_{1-x}Zn_{4-y}Sb₃, respectively.

Diffraction patterns were analyzed by the Rietveld refinement method using the GSAS II software package.⁴⁴ The profile parameters, background parameters, zero correction, and cell parameters were refined first. The background was fitted using a shifted 14 order Chebyshev polynomial function (NaZn₄Sb₃) and 24-point linear interpolation (HT-Na_{1-x}Zn_{4-y}Sb₃), a pseudo-Voigt function was applied to generate the profile shape, and the preferential orientation of crystallites was taken into account. Due to the complexity of the structure of HT-Na_{1-x}Zn_{4-y}Sb₃ phase and presence of light elements (Na, Zn) together with heavy element (Sb), the refinement of all atomic parameters cannot be reliably performed from powder X-ray diffraction data (data/parameters), but full profile fitting using the model determined from the single crystal X-ray diffraction results in low $R_B = 12\%$, indicating its validity (Tables S1, Figure S2).

Spark-Plasma Sintering. Samples of NaZn₄Sb₃ and HT-Na_{1-x}Zn_{4-y}Sb₃ prepared via the hydride route were further consolidated into dense pellets using Spark Plasma Sintering (SPS). In the argon-filled glovebox, the powdered samples were loaded into a small graphite die (inner diameter 5 mm) between several circles of graphite foil and enclosed with tungsten carbide plungers. The smaller die was assembled, inserted into a larger outer graphite die with graphite plungers (inner diameter 20 mm), and further transported to SPS-machine Dr. Sinter Lab Jr. SPS-211Lx (Sumitomo Coal Mining Co., Ltd.) keeping the assembly under inert atmosphere. The samples were sintered by slow heating to 448 K over a period of 10 min under a uniaxial pressure of 90 MPa and dwelling for 5 min. Afterward, the pressure was released, and sintered pellets were allowed to cool to room temperature without application of pressure. The pellets were removed from the graphite dies and polished to remove traces of the graphite foil. The geometrical densities of the pellets were ~85% and 81% for NaZn₄Sb₃ and HT-Na_{1-x}Zn_{4-y}Sb₃ phases, respectively, compared to the theoretical X-ray densities. Binary ZnSb was detected as impurity (7 wt %) in sintered pellet of NaZn₄Sb₃ phase.

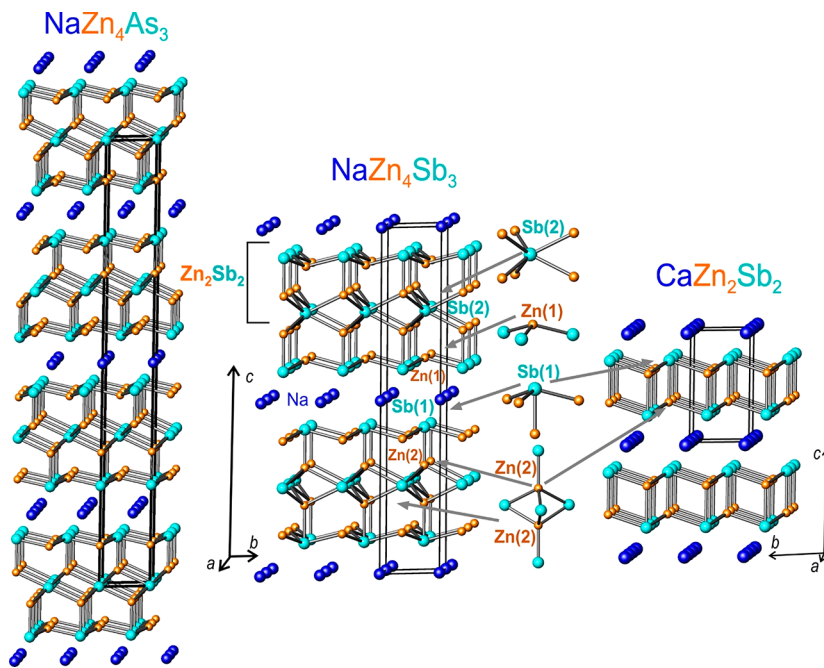


Figure 1. Crystal structure of NaZn_4Sb_3 in comparison with the structures of NaZn_4As_3 (left) and CaZn_2Sb_2 (right). The coordination of Zn and Sb atoms is emphasized; Na(Ca), blue; Zn, orange; and Sb(As), cyan.

Elemental Analysis. Elemental analysis was performed by means of EI Quanta-250 field emission scanning electron microscope (SEM) equipped with an Oxford X-Max 80 detector and an Oxford Aztec energy-dispersive X-ray analysis system. Inside the glovebox small pieces of the pellets sintered by SPS were mounted onto an aluminum holder designed for air-sensitive samples using double-sided carbon tape, oriented with a flat face perpendicular to the beam and analyzed using a 15 kV accelerating voltage and an accumulation time of 60 s.

Thermoelectric Properties Measurement. Transport properties of pellets prepared by SPS were measured in the temperature range of 10–300 K using the commercial multipurpose Physical Properties Measurement System Evercool II (PPMS, Quantum Design). The Seebeck thermopower and thermal conductivity were measured using the Thermal Transport Option (TTO) in a two-probe configuration. Electrical resistivity was measured using the Alternating Current Transport (ACT) option and a four-probe geometry using 50 μm platinum wires attached with silver paste.

Differential Scanning Calorimetry–Thermal Gravimetry Analysis (DSC-TGA). To evaluate the thermal stability of the phases, a differential scanning calorimetry (DSC) measurement was performed using a Netzsch 404 F3 Pegasus differential scanning calorimeter. Powdered samples of NaZn_4Sb_3 and $HT\text{-Na}_{1-x}\text{Zn}_{4-y}\text{Sb}_3$ ($m \cong 50$ mg) were sealed inside an evacuated silica ampule, heated to 873 K, and cooled to room temperature with a rate of 10 K/min rate. In a separate run, the thermal stabilities of a powdered samples of NaZn_4Sb_3 ($m = 12.14$ mg) and $HT\text{-Na}_{1-x}\text{Zn}_{4-y}\text{Sb}_3$ ($m = 11.05$ mg) were checked by DSC/TGA measurement in an alumina Al_2O_3 pan-type crucible with a lid using a Netzsch STA449 F1 Jupiter. Samples were heated to 900 K and cooled to room temperature with a 10 K/min rate under a flow of argon.

Computational Details. First-principles calculations were carried out based on density functional theory (DFT) using the VASP code.^{45–47} The projector augmented-wave (PAW) method⁴⁸ was used to describe the electron–ion interaction, and the generalized gradient approximation (GGA) in the Predew–Burke–Ernzerhof (PBE) form⁴⁹ was employed for the exchange-correlation energy functional. A plane-wave basis with a kinetic energy cutoff of 520 eV was used. Only the Γ -point was used to perform the Brillouin zone integration for the large unit cell with the composition $\text{Na}_{32}\text{Zn}_{124}\text{Sb}_{96}$ containing 252 atoms. All atoms in the calculation cell were allowed to relax until the forces on each atom were smaller than 0.01 eV/ \AA .

RESULTS AND DISCUSSION

In the ternary system Na–Zn–Sb, only NaZnSb (PbClF or Cu_2Sb structure type, $P4/nmm$) has been previously reported.^{50,51} Recently, we successfully utilized the hydride route for preparation of complex solids, including antimoniides,^{20,21} which are hardly accessible by traditional methods of synthesis. The hydride route utilizes brittle salt-like alkali metal hydride precursors (LiH, NaH, KH) instead of ductile and soft alkali metals. This method facilitates thorough mixing of the reactants, allowing for comprehensive control over the alkali metal concentration, thus providing an exceptional purity of products and fast reaction kinetics. Furthermore, it can be used for fast screening of multicomponent systems, allowing identification of new compounds with specific chemical composition. For example, in the K–Zn–Sb system, in which only KZnSb has been previously reported,^{50,51} we recently obtained the new compound $\text{K}_{8-x}\text{Zn}_{18+3x}\text{Sb}_{16}$ with high purity using the hydride method,²⁰ while synthesis from elements resulted in inhomogeneous samples with a considerable fraction of thermodynamically stable KZnSb .

When the same hydride synthesis is applied in the Na–Zn–Sb system, we identified NaZn_4Sb_3 , which subsequently led to the discovery of the $HT\text{-Na}_{1-x}\text{Zn}_{4-y}\text{Sb}_3$ phase. The composition NaZn_4Sb_3 is located directly on the line connecting Na and binary Zn_4Sb_3 or $\text{Zn}_{13-\delta}\text{Sb}_{10}$ in the ternary phase diagram. Interestingly, Zn_4Sb_3 or $\text{Zn}_{13-\delta}\text{Sb}_{10}$ exhibits complex temperature-driven phase transitions $\alpha' \rightarrow \alpha \rightarrow \beta \rightarrow \gamma$ followed by melting at 841 K.^{52–56} From the structural point of view, the phase transitions in Zn_4Sb_3 occur because of the ordering of Zn interstitial atoms and vacancies and are accompanied by the slight variation in Zn composition.^{52–56} Structural polymorphism is retained, when Na is introduced to the Zn_4Sb_3 structure, as two polymorphic-like compounds can be stabilized: NaZn_4Sb_3 and another phase (referred to as $HT\text{-Na}_{1-x}\text{Zn}_{4-y}\text{Sb}_3$). The latter shows a deviation from the 1:4:3 composition and is stable in a narrow temperature range, and

thus can only be prepared by quenching from high temperatures.

Crystal Structure of NaZn_4Sb_3 . Synthesis from Na, Zn, and Sb elements in a 1.03:4:3 molar ratio resulted in inhomogeneous samples, where NaZnSb was a major product. On the contrary, the single-phase sample of NaZn_4Sb_3 can be prepared using NaH , Zn, and Sb mixed in a 1.03:4:3 molar ratio. Synthesis from elements always resulted in inhomogeneous multiphase samples; thus, the compositions utilized for single crystal growth deviate from 1:4:3. Single crystals of the targeted NaZn_4Sb_3 phase were selected from the multiphase sample with nominal molar ratio of $\text{Na}:\text{Zn}:\text{Sb} = 1.7:4.7:3$; samples with composition closer to stoichiometric 1:4:3 molar ratio (e.g., 1.3:4.3:3) contained substantial amounts of NaZnSb and binary zinc antimonides as impurities, making harvesting of crystals challenging (Figure S3). The tentative crystal structure model was first obtained from single crystal X-ray diffraction, but the crystals were of poor quality. The obtained model was further refined using synchrotron powder X-ray diffraction data (Tables 2 and S1). NaZn_4Sb_3 has a layered crystal structure ($P6_3/mmc$, $hP16$, $a = 4.43579(4)$ Å, $c = 23.41553(9)$ Å, $Z = 2$) (Figure 1). Search by Pearson symbol, unit cell metric, and Wyckoff sequence (f^3da) of the Inorganic Structure database (ICSD)⁵⁷ indicates that this is a new structure type, although its crystal structure is closely related to other ternary zinc antimonides, as discussed below. In the structure of NaZn_4Sb_3 , Zn atoms occupy two 4f sites, and Sb atoms one 4f and one 2d site, while a single Na 2a site is present (Table 2). The layered structure of NaZn_4Sb_3 can be

viewed as anionic $[\text{Zn}_4\text{Sb}_3]^-$ slabs sandwiched between a single layer of Na^+ cations. Within the anionic $[\text{Zn}_4\text{Sb}_3]^-$ slab there are two types of Zn atoms: Zn(2) with a distorted tetrahedral coordination by four Sb atoms at a distances of 2.57 and 2.86 Å ($\times 3$) and Zn(1) with a trigonal pyramidal coordination by three Sb atoms at a distance of 2.65 Å. A fourth Sb atom is present for Zn(1) but is located at a considerably longer distance, ~3.18 Å. The two antimony atoms have considerably different environments as well: Sb(1) capping the surface of the slab and Sb(2) at the center of the slab. Sb(1) (4f site) is in an “inverted tetrahedron” or “umbrella-like” coordination by four Zn atoms at distances of 2.65 Å ($\times 3$) and 2.57 Å, and additionally, it has 3 Na atoms at a distance of 3.26 Å. Sb(2) (2d site) is in a trigonal prismatic coordination by six Zn atoms at a distance of 2.86 Å. These distances are within the range for typical Zn–Sb distances in other ternary alkali metal zinc antimonides, such as NaZnSb (2.76 Å),^{21,56} KZnSb (2.62 Å),⁵⁰ $\text{K}_{8-x}\text{Zn}_{18+3x}\text{Sb}_{16}$ (2.63–2.95 Å),²⁰ hex-LiZnSb (2.67–2.76 Å),⁵⁸ and $\text{Rb}_2\text{Zn}_5\text{Sb}_4$ (2.64–2.90 Å at 200 K),⁵⁹ as well as in binary zinc antimonides, such as ZnSb (2.64–2.90 Å),⁶⁰ Zn_4Sb_3 (2.55–2.98 Å),⁵² and $\beta\text{-Zn}_4\text{Sb}_7$ (2.63–3.15 Å).⁶¹

The structure of NaZn_4Sb_3 is related to the well-studied AeZn_2Sb_2 ($\text{Ae} = \text{Ca}, \text{Sr}, \text{Eu}, \text{Yb}$) family^{34,35} with Ce_2SO_2 structure type ($P\bar{3}m$, hPS , for $\text{Ae} = \text{Ca}$, $a = 4.441$ Å and $c = 7.464$ Å) as well as to the ACd_4Pn_3 and AZn_4Pn_3 phases ($\text{A} = \text{Na}, \text{K}, \text{Rb}, \text{Cs}; \text{Pn} = \text{As}, \text{P}$) with NaZn_4As_3 structure type ($R\bar{3}m$, $hR8$, for NaZn_4As_3 , $a = 4.1694$ Å and $c = 32.86$ Å).⁶² Disregarding the trigonal pyramidal coordination of the Zn(1) atom, the anionic $[\text{Zn}_4\text{Sb}_3]^-$ slab in the structure of NaZn_4Sb_3 can be viewed as a layer of edge-sharing ZnSb_4 tetrahedra in the ab -plane, similar to that in AeZn_2Sb_2 . Unlike the AeZn_2Sb_2 structure, the $[\text{Zn}_2\text{Sb}_2]$ layers are further linked by sharing common Sb atoms into $[\text{Zn}_4\text{Sb}_3]$ slabs. In fact, the structure of NaZn_4Sb_3 can be derived from the CaZn_2Sb_2 structure (Figures 1 and 2a), where every other Ca layer is removed and the adjacent $[\text{Zn}_2\text{Sb}_2]$ layers are shifted and condensed into a single slab accompanied by removal of one Sb layer (Figure 2a). The resultant $[\text{Zn}_4\text{Sb}_3]$ slab in NaZn_4Sb_3 is comparable to that of $[\text{Zn}_4\text{As}_3]$ in NaZn_4As_3 (Figure 1, left). Unlike NaZn_4Sb_3 , the two Zn atoms in adjacent tetrahedral ZnAs_4 units are not aligned, leading to a different central Sb

Table 2. Atomic Coordinates and Isotropic Displacement Parameters of NaZn_4Sb_3 ($P6_3/mmc$, $hP16$, $a = 4.43579(4)$ Å, $c = 23.41553(9)$ Å) and Synchrotron Data, 298 K

site	Wyckoff site	x	y	z	U_{iso} Å 2
Sb(1)	4f	1/3	2/3	0.08580(4)	0.0105(2)
Sb(2)	2d	1/3	2/3	3/4	0.0220(3)
Zn(1)	4f	1/3	2/3	0.61404(5)	0.0350(4)
Zn(2)	4f	1/3	2/3	0.19542(5)	0.0361(3)
Na	2a	0	0	0	0.112(3)

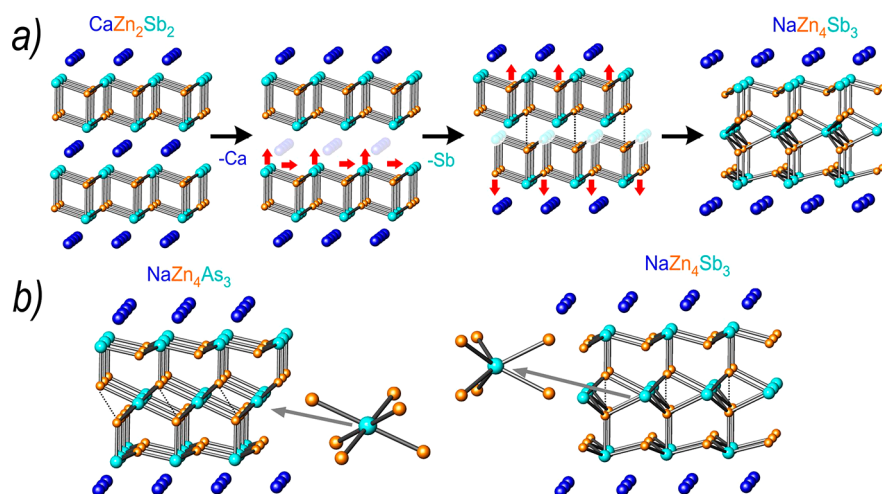


Figure 2. (a) Schematic showing the transformation of the $[\text{Zn}_2\text{Sb}_2]$ layer in the CaZn_2Sb_2 structure into the $[\text{Zn}_4\text{Sb}_3]$ layer in structure of NaZn_4Sb_3 . (b) Structural comparison of anionic slabs $[\text{Zn}_4\text{As}_3]$ and $[\text{Zn}_4\text{Sb}_3]$; the dashed lines emphasize the alignment of Zn atoms within two stacked $\text{Zn}(\text{As}/\text{Sb})_4$ tetrahedral units. The difference in coordination polyhedral for Sb(As) is shown. Na(Ca), blue; Zn, orange; and Sb(As), cyan.

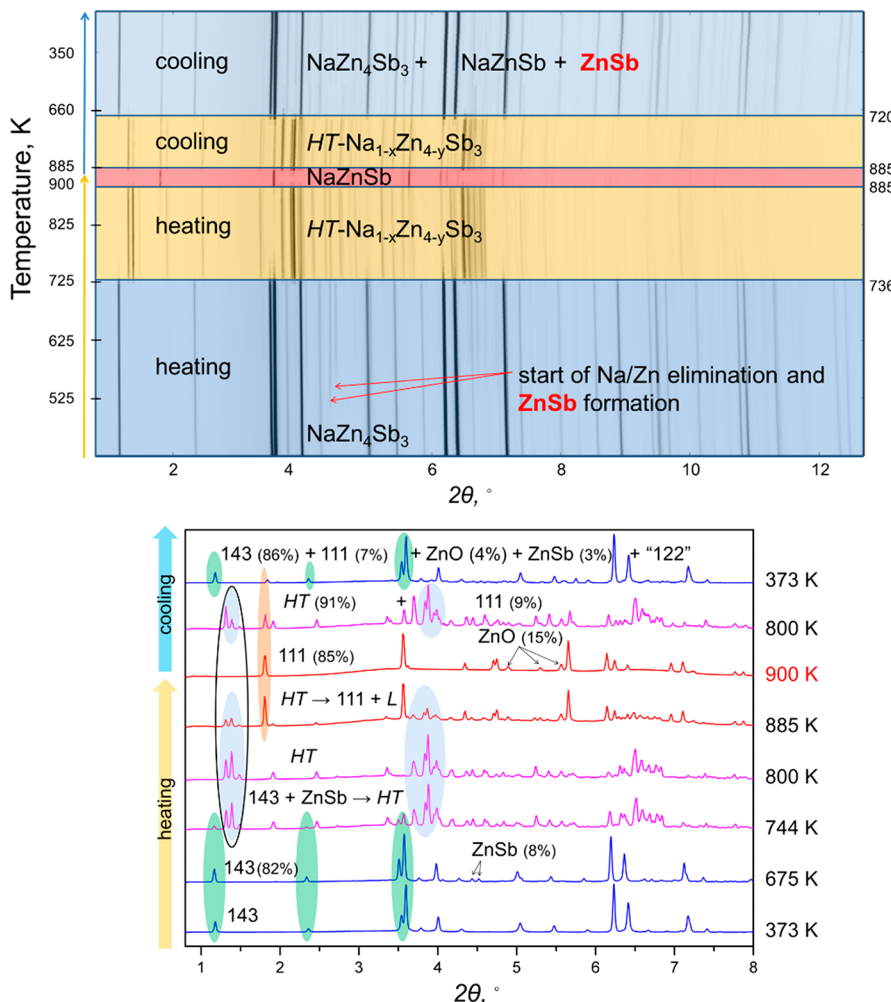


Figure 3. (top) High-temperature in situ powder X-ray diffraction patterns, showing the transformation of powdered sample NaZn_4Sb_3 sealed in an evacuated silica capillary. The “waterfall” plot shows the evolution of PXRD patterns with the concomitant change in temperature from room temperature to 900 K followed by subsequent cooling to room temperature. The temperature regions with distinct phase contributions are highlighted in blue/yellow/red. (bottom) Selected high-temperature powder X-ray diffraction patterns showing the products of decomposition/transformation of the NaZn_4Sb_3 at different temperatures. Selected groups of peaks as “fingerprints” of the ternary and binary phases are highlighted: green (143), NaZn_4Sb_3 ; blue (HT), $\text{HT-Na}_{1-x}\text{Zn}_{4-y}\text{Sb}_3$; orange, (111), NaZnSb ; L = liquid; and (122), “ NaZn_2Sb_2 ”.

atom coordination: trigonal prismatic in the case of NaZn_4Sb_3 and trigonal antiprismatic in NaZn_4As_3 (Figure 2b). Furthermore, the stacking sequence of the $[\text{Zn}_4(\text{As/Sb})_3]$ slabs is different: in NaZn_4As_3 the adjacent $[\text{Zn}_4\text{As}_3]$ slabs are shifted by $1/3$ in the ab -plane, to produce an *R*-centered trigonal unit cell, while in NaZn_4Sb_3 the two $[\text{Zn}_4\text{Sb}_3]$ slabs are related by an inversion center with hexagonal layers of Na^+ cations in between. Therefore, the NaZn_4Sb_3 is a new representative for the family of Zintl phases which adopts a 1:4:3 stoichiometry but has its own unique layered crystal structure.

Considering Na and Zn as +1 and +2 cations, respectively, and the electronegative Sb having -3 oxidation state, the valence electron count for NaZn_4Sb_3 yields electron-balanced composition $\text{Na}^+(\text{Zn}^{2+})_4(\text{Sb}^{3-})_3$.

Reversible NaZn_4Sb_3 to $\text{HT-Na}_{1-x}\text{Zn}_{4-y}\text{Sb}_3$ Transformation by In Situ HT-PXRD. High-temperature synchrotron powder X-ray diffraction (HT-PXRD) of the NaZn_4Sb_3 sample sealed under vacuum in a silica capillary indicates its structural transformation into the $\text{HT-Na}_{1-x}\text{Zn}_{4-y}\text{Sb}_3$ phase at ~ 736 K (Figure 3). Binary ZnSb begins to emerge at ~ 500 K

upon heating, indicating partial Na elimination as a result of side reaction with the silica, but disappears (melts) above 736 K. With further heating of $\text{HT-Na}_{1-x}\text{Zn}_{4-y}\text{Sb}_3$ above 885 K, the sample converts to NaZnSb and melt. Upon cooling from 900 K, the reversible transformation takes place: $\text{NaZnSb} + \text{melt} \rightarrow \text{HT-Na}_{1-x}\text{Zn}_{4-y}\text{Sb}_3$ at 885 K $\rightarrow \text{NaZn}_4\text{Sb}_3$ at 720 K. It should be noted that, according to the HT-PXRD data, the *HT*-phase exists exclusively in the narrow temperature range 736–885 K. With the increasing of temperature above ~ 736 K, formation of the *HT*-phase is driven by Na/Zn elimination, and as a result its content increases, while a fraction of the NaZn_4Sb_3 -phase decreases. Above 810 K, traces of NaZnSb appear, which become more pronounced above 885 K when the *HT*-phase completely decomposes. By comparing two PXRD patterns collected at 373 K on heating and cooling steps, the cooling step contains NaZn_4Sb_3 ($\sim 86\%$) with more impurities, such as NaZnSb , ZnSb , and unassigned peaks, compared to heating data (i.e., initial sample). This suggests a shift in composition from the initial 1:4:3 Na:Zn:Sb ratio and partial decomposition of NaZn_4Sb_3 phase upon heating (Figures 3 and 6).

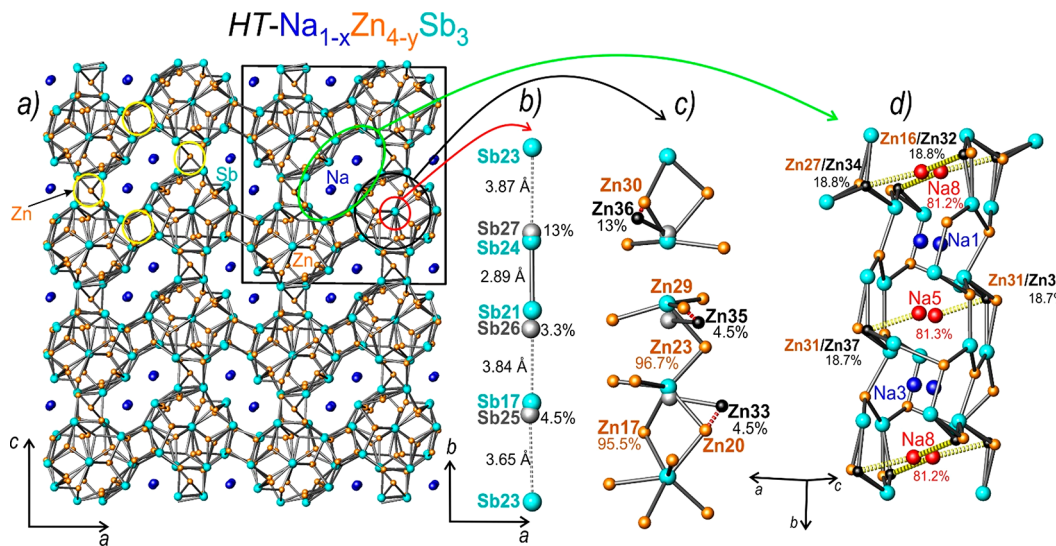


Figure 4. (a) Crystal structure of $HT\text{-Na}_{1-x}\text{Zn}_{4-y}\text{Sb}_3$ in the ac -plane: Na, blue; Zn, orange; and Sb, cyan. Split sites are not shown, and various fragments are highlighted with red (Sb chains), green (Na channels), yellow, and black circles. (b) Sb chain running along the b -axis; split Sb sites are shown in gray, and their s.o.f. is given in %; the bond distances and longer interatomic distances are drawn with solid and dashed lines, respectively. (c) Coordination of Sb atoms from the chain by Zn atoms; the split Zn sites are shown in black, and their s.o.f. is given in %; the unrealistic Zn–Zn distances due to the split sites are shown with red dashed lines. (d) Coordination of Na atoms within the channel; Na with partial occupancy is shown in red together with its s.o.f. (%); the split Zn sites are shown in black, and their s.o.f. is given in %; the unrealistic Na–Zn distances due to the split sites are shown with yellow dashed lines. Na–Na distances exceed 3.59 Å.

In situ high-temperature synchrotron powder X-ray diffraction is very sensitive to phase transitions, as it provides high resolution data, facilitating detection of even small amounts of crystalline phase(s) at different temperatures. Differential scanning calorimetry (DSC) on the other hand is not suitable for systems where many exo- and endothermic reactions take place simultaneously. The Na–Zn–Sb system is an example of such a case, in which samples that are heat treated under vacuum can lead to partial Na/Zn evaporation and possibly side reactions with the containment vessel (silica). DSC data of the NaZn_4Sb_3 sample in an alumina crucible (Figure S4) indicates an endothermic process, possibly due to its melting or decomposition at ~ 750 K, followed by a smaller endothermic event at ~ 800 K, possibly because of NaZnSb formation. Upon heating of the sample in an alumina crucible, a 1% mass loss is observed, which may be due to a slight Na/Zn evaporation. On cooling, two exothermic peaks are observed: less intensive at ~ 765 K, possibly due the traces of $HT\text{-Na}_{1-x}\text{Zn}_{4-y}\text{Sb}_3$ present, as a result of the composition shift, and a more intense peak at ~ 735 K, when NaZn_4Sb_3 is recovered. In turn, DSC data of samples run in silica is in accordance with in situ high-temperature synchrotron powder X-ray diffraction data. The PXRD data of the sample after DSC (in silica) indicates that NaZn_4Sb_3 is partially decomposed during the measurement, as peaks of Zn_4Sb_3 and ZnO are evident (Figure S5). This is further evidence that Na elimination processes may be due to a side reaction with the silica vessel.

Synthesis of $HT\text{-Na}_{1-x}\text{Zn}_{4-y}\text{Sb}_3$. Equipped with the knowledge regarding the temperature range, where $HT\text{-Na}_{1-x}\text{Zn}_{4-y}\text{Sb}_3$ is stable, its synthesis was performed by quenching of the NaZn_4Sb_3 sample in an evacuated and sealed silica ampule from 800 K. Furthermore, the $HT\text{-Na}_{1-x}\text{Zn}_{4-y}\text{Sb}_3$ compound can be prepared by annealing of NaH , Zn, and Sb in the Ta ampule, but only when the Na- and Zn-depleted composition $\text{NaH:Zn:Sb} = 0.93:3.61:3$ (molar

ratio) is used, whereas 1.03:4:3 molar ratio always gives the NaZn_4Sb_3 phase even after quenching from 800 K. This again indicates that during heating of NaZn_4Sb_3 in the silica tube partial elimination of Na and Zn takes place, probably due to the side reaction of Na with SiO_2 , thus shifting the composition toward the Na/Zn depleted facilitates formation of $HT\text{-Na}_{1-x}\text{Zn}_{4-y}\text{Sb}_3$. The Na/Zn deficiency in the $HT\text{-Na}_{1-x}\text{Zn}_{4-y}\text{Sb}_3$ phase was further confirmed by refinement of the crystal structure from single crystal diffraction data and EDX analysis (vide infra).

Crystal Structure of $HT\text{-Na}_{1-x}\text{Zn}_{4-y}\text{Sb}_3$: Structural Complexity and Disorder. Single crystals were selected from an inhomogeneous sample prepared from the elements in the same nominal composition ($\text{Na:Zn:Sb} = 1.7:4.7:3$) as one used for crystal growth of the NaZn_4Sb_3 compound; the sample was quenched to stabilize $HT\text{-Na}_{1-x}\text{Zn}_{4-y}\text{Sb}_3$. The sample contained a considerable fraction of NaZnSb impurity (in a powdery form), while chunks mechanically separated from powders comprise mainly the $HT\text{-Na}_{1-x}\text{Zn}_{4-y}\text{Sb}_3$ phase (Figure S6). The complex crystal structure (Figure 4) of $HT\text{-Na}_{1-x}\text{Zn}_{4-y}\text{Sb}_3$ was determined from single crystal X-ray diffraction data. $HT\text{-Na}_{1-x}\text{Zn}_{4-y}\text{Sb}_3$ crystallizes in the monoclinic space group $P2_1/c$ (No. 14) and has a unit cell with monoclinic, pseudo-orthorhombic symmetry ($a = 19.508(3)$ Å, $b = 14.708(3)$ Å, $c = 20.736(4)$ Å, $\beta = 90.402(5)^\circ$) (Table 1). The unit cell of the ideal structure contains 96 Sb atoms distributed over 24 4e-sites, 124 Zn atoms distributed over 31 4e-sites, and 32 Na atoms occupying 8 4e-sites (Table 2). Searching of the Inorganic Crystal Structure Database (ICSD)⁵⁷ using the Pearson symbol ($mP252$), unit cell metrics, and Wyckoff sequence (e^{63}) indicate that this is a new structure type.

The structure is organized around Sb chains running along the b -axis (Figure 4a,b). These chains are surrounded by Zn atoms, which are further connected to a second shell of Sb atoms, forming tubular columns along the b -axis (Figure 4a,c).

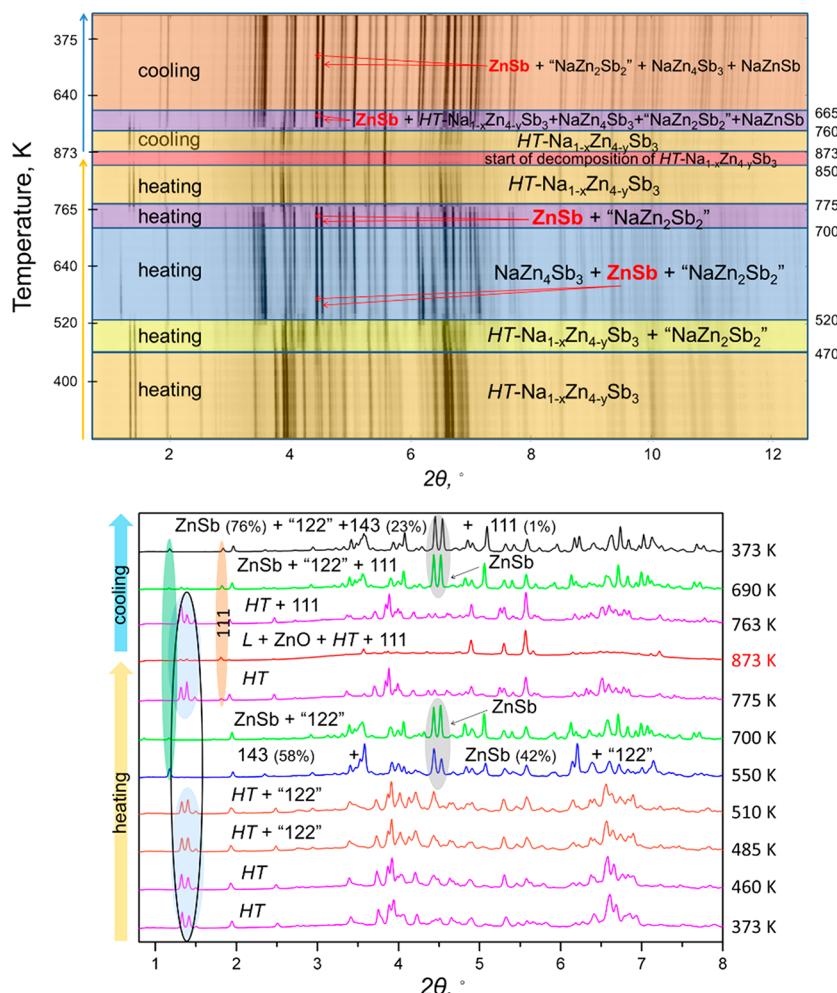


Figure 5. (Top) High-temperature in situ X-ray diffraction patterns, showing the transformation of the powdered sample of $HT\text{-Na}_{1-x}\text{Zn}_{4-y}\text{Sb}_3$ sealed into an evacuated silica capillary. The “waterfall” plot shows the evolution of powder XRD patterns with the change in temperature from room temperature to 873 K followed by subsequent cooling to room temperature. The temperature regions with distinct phase contributions are highlighted in blue/yellow/purple/red/orange. (bottom) Selected high temperature powder X-ray diffraction patterns showing the products of decomposition/transformation of the $HT\text{-Na}_{1-x}\text{Zn}_{4-y}\text{Sb}_3$ at different temperatures. Selected groups of peaks as “fingerprints” of the ternary and binary phases are highlighted: green (143), NaZn_4Sb_3 ; blue (HT), $HT\text{-Na}_{1-x}\text{Zn}_{4-y}\text{Sb}_3$; orange (111), NaZnSb ; gray, ZnSb; (122), “ NaZn_2Sb_2 ”.

Those columns are then linked in the *ac*-plane either via Zn–Sb intercolumnar bonds or via bridging Zn atoms to form a three-dimensional framework with large channels, hosting two columns of Na^+ cations (Figure 4d). The Zn–Sb distances range between 2.57 Å and 2.94 Å and are similar to the Zn–Sb distances in other ternary alkali metal zinc antimonides (vide supra). The Sb atoms are either 4, 5-, or 6-coordinated by Zn atoms (Table S3). Sb atoms surround Na within the channels and, thus, are coordinated by 2–4 Na^+ at distances ranging from 3.13 to 3.67 Å. The relatively short Na–Sb distances of ~3.13 Å are not typical but have been reported in other ternary and quaternary sodium antimonides, such as Na_3InSb_2 ,⁶³ $\text{Na}_2\text{Al}_2\text{Sb}_3$,⁶⁴ Na_5SnSb_3 ,⁶⁵ $\text{K}_2\text{NaInSb}_2$,⁶⁶ and $\text{Na}_2\text{YbCdSb}_2$.⁶⁷ Most of the Zn atoms are in a distorted tetrahedral coordination by four Sb sites, except for zinc atoms residing in split positions.

A considerable degree of disorder occurs within the structure of $HT\text{-Na}_{1-x}\text{Zn}_{4-y}\text{Sb}_3$, mainly associated with the Na(5) and Na(8) sites being ~81% occupied, as well as Sb and Zn split sites and two partially occupied zinc sites, Zn(23) and Zn(17) (Figure 4b,d). Split sites within the Sb chain (Figure 4b,c) evoke additional splitting in adjacent Zn sites. For

instance, when Sb(24) is present, it is coordinated by Zn(30), while Sb(27) is coordinated by Zn(36). Likewise Sb(17), Zn(20), and Zn(17) atoms (s.o.f. of 95.5%) or Sb(25) and Zn(33) atoms (s.o.f. of 4.5%) are present. The partial occupancy of Na(5) and Na(8) within the channels also leads to the splitting of the adjacent Zn positions; e.g., when Na is absent, Zn atoms slightly move toward the “hole” in the channel: either Na(5) and Zn(31) (s.o.f. 81.4%) or Zn(37) (s.o.f. 18.7(9)%)) are present. Similarly, when Na(8), Zn(16), and Zn(27) are occupied (s.o.f. 81.2%), then Zn(32) and Zn(34) are absent (s.o.f. 18.8%). Considering structural disorder, the refined composition from single crystal XRD for $HT\text{-Na}_{1-x}\text{Zn}_{4-y}\text{Sb}_3$ is $\text{Na}_{0.953(3)}\text{Zn}_{3.865(1)}\text{Sb}_3$, which is consistent with the Na- and Zn-depleted composition needed for synthesis. This refined composition $HT\text{-Na}_{1-x}\text{Zn}_{4-y}\text{Sb}_3$ suggests an electron imbalance, when +1 and +2 charges are assigned for Na and Zn, respectively, and the electronegative Sb has a -3 charge: $(\text{Na}^+)^{0.953}(\text{Zn}^{2+})^{3.865}(\text{Sb}^{3-})_3$ with 0.36 extra electrons per formula unit.

Vacancy Formation in $HT\text{-Na}_{1-x}\text{Zn}_{4-y}\text{Sb}_3$: Computational Input. In order to evaluate the preference for the vacancy formation in the specific Na sites in the structure of

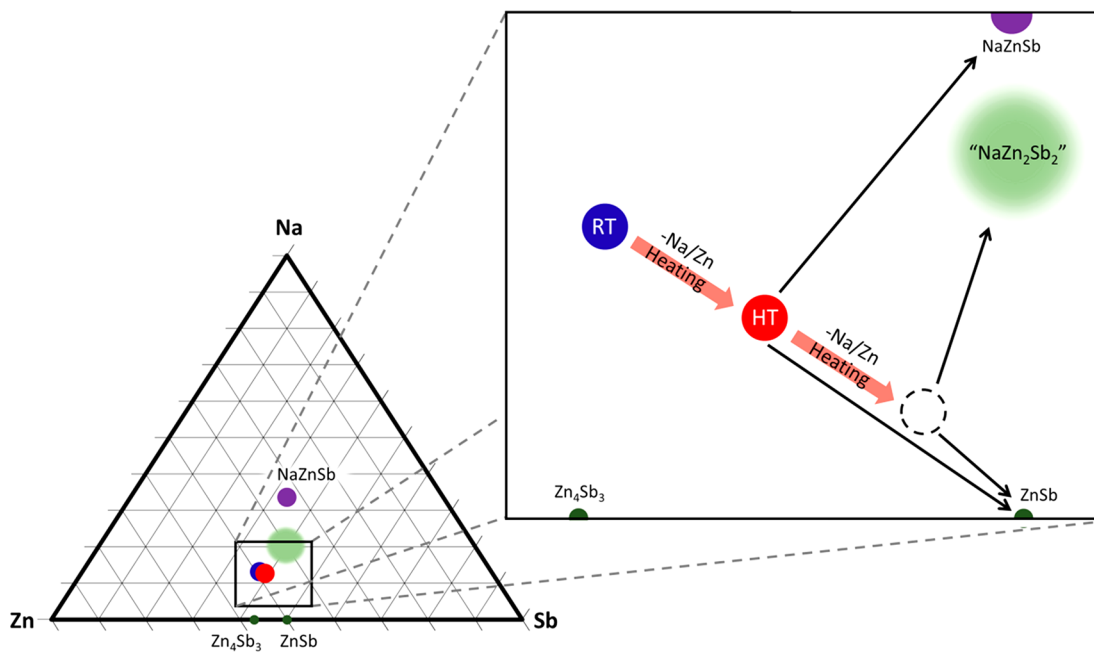


Figure 6. Schematic of the compositional ternary phase diagram for Na–Zn–Sb. Compositional shift along the line of transformation from NaZn_4Sb_3 (blue circle) and $\text{HT-Na}_{1-x}\text{Zn}_{4-y}\text{Sb}_3$ (red circle) during heating in a silica capillary. The 1:4:3 composition of NaZn_4Sb_3 is being shifted during heating due to Na/Zn elimination; therefore, the $\text{HT-Na}_{1-x}\text{Zn}_{4-y}\text{Sb}_3$ phase with Na/Zn depleted composition can be stabilized. The initial composition of the sample of $\text{HT-Na}_{1-x}\text{Zn}_{4-y}\text{Sb}_3$ phase is shifted during its heating, and then unknown phase referred as “ NaZn_2Sb_2 ” shows up on the phase equilibria.

$\text{HT-Na}_{1-x}\text{Zn}_{4-y}\text{Sb}_3$, the vacancy formation energies (E_{vac}) for various Na sites were calculated by

$$E_{\text{vac}} = E(\text{cell}_{\text{vac}}) + E(\text{Na}) - E(\text{cell})$$

where $E(\text{cell})$ and $E(\text{cell}_{\text{vac}})$ are the total energies of the optimized structures with and without a Na vacancy, respectively. $E(\text{Na})$ is the energy of a Na atom in the bulk phase. The idealized structure model (without split sites for Sb/Zn) considered for calculations has the composition $\text{Na}_{32}\text{Zn}_{124}\text{Sb}_{96}$ ($\equiv \text{NaZn}_{3.875}\text{Sb}_3$, cell) and was further optimized to yield $E(\text{cell})$. One Na atom was removed from each of the eight Na sites in succession (Table 3), and the structure with

occupancies (Table S2). Furthermore, based on the first-principle calculations, the formation of vacancies at Na(5) and Na(8) sites only causes slight local structural relaxations. The relaxation patterns around vacant Na(5) or Na(8) are rather similar: vacancy formation causes two adjacent Zn atoms and adjacent Na atoms to shift toward the vacancy, while the overall structural motif remains unchanged. That is again consistent with the structure solved from SC XRD data (Figure 4d), where vacancies in Na(5) and Na(8) sites cause the splitting of the adjacent Zn sites.

Thermal Stability of $\text{HT-Na}_{1-x}\text{Zn}_{4-y}\text{Sb}_3$. High-temperature powder XRD data for the $\text{HT-Na}_{1-x}\text{Zn}_{4-y}\text{Sb}_3$ phase indicates multiple transitions upon heating (Figure 5). A cascade of exothermic peaks is present on the DSC heating curve in an alumina crucible at 470–575 K (Figure S4), indicating that the HT -phase is indeed metastable at room temperature and its early transformation to NaZn_4Sb_3 was observed already at 520 K. The metastable nature of $\text{HT-Na}_{1-x}\text{Zn}_{4-y}\text{Sb}_3$ was also evident from its decomposition during spark plasma sintering already at 473 K, while sintering at a slightly lower temperature (453 K) resulted in 81% pellet compactness without any discernible changes based on PXRD.

From the in situ high-temperature synchrotron powder XRD data (Figure 5) the HT -phase was found to decompose according to the following equation: $\text{HT-Na}_{1-x}\text{Zn}_{4-y}\text{Sb}_3 \rightarrow \text{NaZn}_4\text{Sb}_3 + \text{ZnSb} + \text{“NaZn}_2\text{Sb}_2\text{”}$ in the temperature range 470 K–765 K. A new phase detected from synchrotron PXRD data has a composition richer in Na and Sb than 1:4:3; this phase will be reported in due course (tentative composition is ~ 122). Upon further heating above 765 K, the $\text{HT-Na}_{1-x}\text{Zn}_{4-y}\text{Sb}_3$ phase reappears (also evident from DSC data, Figure S4) as a strong endothermic peak at 770 K, according to the following equation: $\text{NaZn}_4\text{Sb}_3 + \text{ZnSb} + \text{“NaZn}_2\text{Sb}_2\text{”} \rightarrow \text{HT-Na}_{1-x}\text{Zn}_{4-y}\text{Sb}_3$. At around 850 K, the decomposition of HT -

Table 3. Vacancy Formation Energy at Each Na Site in the Structure of $\text{HT-Na}_{1-x}\text{Zn}_{4-y}\text{Sb}_3$ ^a

site	E_{vac} (eV)
Na(1)	0.788
Na(2)	0.805
Na(3)	0.902
Na(4)	0.913
Na(5)	0.706
Na(6)	0.917
Na(7)	0.881
Na(8)	0.763

^aThe two sites with the lowest vacancy formation energies are italicized.

the composition $\text{Na}_{31}\text{Zn}_{124}\text{Sb}_{96}$ ($\equiv \text{Na}_{0.96875}\text{Zn}_{3.875}\text{Sb}_3$, cell_{vac}) was optimized to yield $E(\text{cell}_{\text{vac}})$. A positive value of E_{vac} indicates an energy cost to create the vacancy. As it can be seen from Table 3, vacancies at the Na(5) and Na(8) sites have the lowest formation energy compared to other Na sites, which is consistent with the experimentally determined structure from SC XRD with only Na(5) and Na(8) sites exhibiting partial

$\text{Na}_{1-x}\text{Zn}_{4-y}\text{Sb}_3$ starts according to DSC data, but the melting temperature of 885 K was not achieved in the HT-PXRD data. Upon cooling, $\text{HT-Na}_{1-x}\text{Zn}_{4-y}\text{Sb}_3$ recovers, and with further cooling to room temperature transforms to NaZn_4Sb_3 , binary ZnSb, and a new phase “ NaZn_2Sb_2 ”; this transformation occurs within broad range of 760–665 K. At the end of the cooling cycle, binary ZnSb is the main product (Figure 5), which indicates that considerable Na/Zn elimination during heating at high temperatures took place, leading to the shift in composition, as schematically represented in Figure 6. DSC data of samples run in silica and alumina are in accordance with in situ HT-PXRD data. A more substantial shift in composition caused by a more pronounced Na/Zn elimination in silica may lead to formation of intermediate side products, leading to the additional DSC peaks on cooling. It should be noted that relative intensities of the peaks of the $\text{HT-Na}_{1-x}\text{Zn}_{4-y}\text{Sb}_3$ phase (apparently visible at $2\theta \sim 1.4^\circ$ in Figure 5) vary at different temperatures, although PXRD of the quenched samples is always same. This could be due to the certain variation in composition or disorder occurring at the different temperatures, while the quenched $\text{HT-Na}_{1-x}\text{Zn}_{4-y}\text{Sb}_3$ always retains its stable configuration.

Figure 6 represents schematically a compositional shift from NaZn_4Sb_3 to the $\text{HT-Na}_{1-x}\text{Zn}_{4-y}\text{Sb}_3$ and finally to the new phase “ NaZn_2Sb_2 ” as a result of a continuous Na/Zn elimination during heating. Upon heating, NaZn_4Sb_3 transforms to $\text{HT-Na}_{1-x}\text{Zn}_{4-y}\text{Sb}_3$, and with further heating, i.e., further Na/Zn elimination, NaZnSb appears on phase equilibria. The composition of the $\text{HT-Na}_{1-x}\text{Zn}_{4-y}\text{Sb}_3$ phase is already Na/Zn depleted compared to that of NaZn_4Sb_3 ; therefore, upon heating of $\text{HT-Na}_{1-x}\text{Zn}_{4-y}\text{Sb}_3$, composition further shifts allowing for the crystallization of a “ NaZn_2Sb_2 ” phase together with a considerable amount of binary ZnSb, indicating considerable deviation from initial 1:4:3 composition.

Elemental Analysis of NaZn_4Sb_3 and $\text{HT-Na}_{1-x}\text{Zn}_{4-y}\text{Sb}_3$. Scanning electron microscopy (SEM) images using backscattered electron (BSE) and secondary electron (SE) modes were collected for the polished pellets sintered by SPS for both NaZn_4Sb_3 and the HT-phase (Figure 7). Compositions were determined by energy-dispersive X-ray (EDX) analysis using 8–11 different areas for each sample. The elemental distribution appears to be homogeneous, and the average compositions were found to be $\text{Na:Zn:Sb} = 1.83(9):3.66(8):3.00(9)$ for NaZn_4Sb_3 and $\text{Na:Zn:Sb} = 1.50(9):3.5(1):3.00(9)$ for the $\text{HT-Na}_{1-x}\text{Zn}_{4-y}\text{Sb}_3$ phase, respectively. Na/Zn is overestimated because of the overlap between Na-K_α and Zn-L_α lines, leading to the difficulties in deconvoluting Na and Zn characteristic lines in the EDX spectrum. Similar inconsistency was seen for the stoichiometric NaZnSb , with the Na:Zn:Sb ratio as determined by EDX of 1.3:1.1.²¹ More importantly, the compositions determined by EDX analysis indicates the lower Zn and Na content in the case of the $\text{HT-Na}_{1-x}\text{Zn}_{4-y}\text{Sb}_3$ phase as compared to NaZn_4Sb_3 , which is consistent with the structure of $\text{HT-Na}_{1-x}\text{Zn}_{4-y}\text{Sb}_3$ determined from SC XRD data as well as Na/Zn depleted composition required for its synthesis.

Low-Temperature Transport Properties of NaZn_4Sb_3 and $\text{HT-Na}_{1-x}\text{Zn}_{4-y}\text{Sb}_3$. The temperature dependence of thermoelectric properties (Figure 8) in the 10–300 K temperature range has been measured for the SPS sintered pellets of NaZn_4Sb_3 (compactness of 85%; 7 wt % of ZnSb impurity) and $\text{HT-Na}_{1-x}\text{Zn}_{4-y}\text{Sb}_3$ (compactness 81%). Elec-

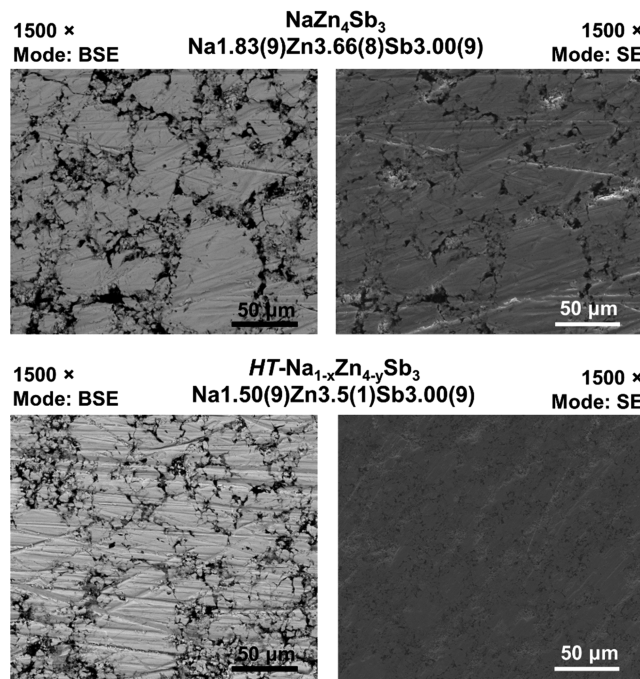


Figure 7. Scanning electron microscopy (SEM) images obtained in backscattered electron (BSE, left) and secondary electron (SE, right) modes for the samples of NaZn_4Sb_3 (top) and $\text{HT-Na}_{1-x}\text{Zn}_{4-y}\text{Sb}_3$ (bottom) prepared via hydride route and further densified by SPS. The compositions of NaZn_4Sb_3 and $\text{HT-Na}_{1-x}\text{Zn}_{4-y}\text{Sb}_3$ phases determined by EDXS and averaged for the 8–11 different areas of each sample.

trical resistivities for both compounds are slightly temperature dependent but exhibit different types of behavior with increasing temperature. The electrical resistivity of the NaZn_4Sb_3 decreases from 2400 m Ω ·cm to 1200 m Ω ·cm with increasing temperature, indicative of a heavily doped semiconductor. On the other hand, the electrical resistivity of the $\text{HT-Na}_{1-x}\text{Zn}_{4-y}\text{Sb}_3$ phase is overall ~ 2 orders of magnitude lower than its NaZn_4Sb_3 counterpart and increases from 33 m Ω ·cm to 36 m Ω ·cm with increasing temperature, a dependence similar to that of a metal.

Both materials have positive Seebeck coefficients which steadily increase with temperature up to 40 and 50 $\mu\text{V K}^{-1}$ at 300 K for $\text{HT-Na}_{1-x}\text{Zn}_{4-y}\text{Sb}_3$ and NaZn_4Sb_3 phases, respectively. This is consistent with *p*-type and holes as charge carriers. Lower overall Seebeck coefficient for $\text{HT-Na}_{1-x}\text{Zn}_{4-y}\text{Sb}_3$ and lower electrical resistivity with the metal-like temperature dependence agree with its more metallic character, compared to NaZn_4Sb_3 . Furthermore, the Na/Zn deficiency in $\text{HT-Na}_{1-x}\text{Zn}_{4-y}\text{Sb}_3$ would be responsible for the more metallic nature of $\text{HT-Na}_{1-x}\text{Zn}_{4-y}\text{Sb}_3$ as compared to formally charge-balanced $\text{Na}^+(\text{Zn}^{2+})_4(\text{Sb}^{3-})_3$. Two orders of magnitude difference in resistivity for NaZn_4Sb_3 and $\text{HT-Na}_{1-x}\text{Zn}_{4-y}\text{Sb}_3$ and a subtle difference in Seebeck coefficients suggests that the variation in band structure plays a significant role in determining electronic transport of these structurally different and compositionally similar compounds.

The total thermal conductivity κ_{total} has contributions from charge carriers, κ_e (electronic thermal conductivity), and a lattice, κ_L (the lattice thermal conductivity): $\kappa_{\text{total}} = \kappa_e + \kappa_L = LT/(\rho + \kappa_L)$, where L is the Lorenz number and ρ is resistivity. For the metals and degenerate semiconductors with high carrier concentrations, the Lorenz number approaches the

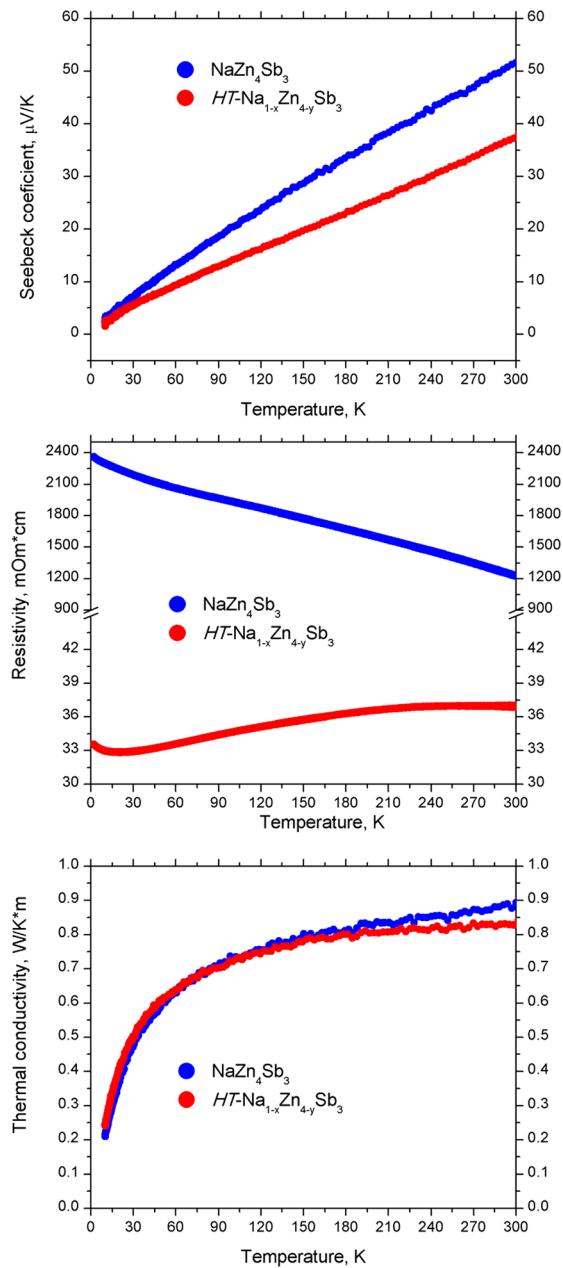


Figure 8. Temperature dependence of transport properties for NaZn_4Sb_3 (blue) and $\text{HT-Na}_{1-x}\text{Zn}_{4-y}\text{Sb}_3$ (red): (top) electrical resistivity; (middle) Seebeck coefficient; and (bottom) thermal conductivity (the estimated electronic thermal conductivity contribution is negligible less than 0.1% for the NaZn_4Sb_3 phase and less than 2.5% for the $\text{HT-Na}_{1-x}\text{Zn}_{4-y}\text{Sb}_3$ phase).

Sommerfeld limit, and $L = 2.45 \times 10^{-8} \text{ W } \Omega \text{ K}^{-2}$ (free electron model). The L estimated using experimental Seebeck coefficients⁶⁸ yields similar values of L within the $2.15\text{--}2.48 \times 10^{-8} \text{ W } \Omega \text{ K}^{-2}$ range for $\text{HT-Na}_{1-x}\text{Zn}_{4-y}\text{Sb}_3$ and NaZn_4Sb_3 phases in the $300\text{--}10 \text{ K}$ temperature range. Thus, the conservative value of $L = 2.45 \times 10^{-8} \text{ W } \Omega \text{ K}^{-2}$ was used. The estimated contribution of the electronic thermal conductivity into the total thermal conductivity is less 0.1% and less the 2.5% for the NaZn_4Sb_3 and $\text{HT-Na}_{1-x}\text{Zn}_{4-y}\text{Sb}_3$ phases, respectively. The thermal conductivity of both phases increases with temperature from $0.2 \text{ W m}^{-1} \text{ K}^{-1}$ to $0.9 \text{ W m}^{-1} \text{ K}^{-1}$ at 300 K . Both NaZn_4Sb_3 ($N_{\text{cell}} = 16$ atoms; $V_{\text{cell}} = 394.2 \text{ \AA}^3$) and structurally more complex $\text{HT-Na}_{1-x}\text{Zn}_{4-y}\text{Sb}_3$ ($N_{\text{cell}} =$

192 atoms; $V_{\text{cell}} = 5986.1 \text{ \AA}^3$) have low thermal conductivity. The layered structure of NaZn_4Sb_3 may favor a high density of stacking faults similar to the SrZnSb_2 , where the boundary scattering was found to reduce thermal conductivity by approximately 30% at room temperature as compared to structurally related SrZn_2Sb_2 .^{31,32} Additionally, the low thermal conductivity could partially be attributed to the lower pellet densities of measured samples (81% and 85%). Moreover, both compounds are lacking the peak in thermal conductivity at lower temperatures. Such a peak is typical for temperature dependence of thermal conductivity of crystalline insulating/semiconducting solids.^{69,70} Such “glass-like” temperature dependence of thermal conductivity, typical for amorphous materials, suggests that the disordered complex crystal structure as in $\text{HT-Na}_{1-x}\text{Zn}_{4-y}\text{Sb}_3$ and “rattling” of Na atoms in the interlayer space in the crystal structure of NaZn_4Sb_3 (Na atom has large ADPs, Table 2) can be responsible for the phonon scattering at low temperatures.

The thermoelectric figure-of-merit zT at room temperature amounts to 7.3×10^{-5} for NaZn_4Sb_3 and to 1.4×10^{-3} for $\text{HT-Na}_{1-x}\text{Zn}_{4-y}\text{Sb}_3$. The low zT for both compounds can be attributed to low Seebeck coefficient and high electrical resistivity, especially in the case of formally charge balanced NaZn_4Sb_3 . Aliovalent substitutions in the NaZn_4Sb_3 compound (for instance, Na for Ca) may lead to an increase of carrier concentration and decrease of its high resistivity.

CONCLUSIONS

In situ synchrotron powder diffraction analysis provided a “panoramic view” on the ternary phases in the Na–Zn–Sb system. Two compositionally similar but structurally different phases NaZn_4Sb_3 and $\text{HT-Na}_{1-x}\text{Zn}_{4-y}\text{Sb}_3$ were detected on phase equilibria below and above 736 K , respectively. The HT -phase can be prepared by quenching samples from high temperatures only if the Na- and Zn-depleted composition is used for synthesis. Moreover, in situ powder X-ray diffraction experiments show an additional ternary phase, stabilized due to considerable Na/Zn elimination under vacuum at elevated temperatures. The structure and properties of this phase will be reported in due course. Transport properties measurements of the NaZn_4Sb_3 and $\text{HT-Na}_{1-x}\text{Zn}_{4-y}\text{Sb}_3$ phases show low thermal conductivities at room temperature of $0.9 \text{ W m}^{-1} \text{ K}^{-1}$. Both polymorphs exhibit moderate positive Seebeck coefficients of $40\text{--}50 \mu\text{V K}^{-1}$ at 300 K , indicative of *p*-type conduction. The observed resistivities differ by 2 orders of magnitude, possibly indicating complex transport behaviors. The presented here synthetic hydride approach coupled with in situ high-temperature powder X-ray diffraction allows for the fast compositional and temperature screening of the phase space, leading to the discovery of the phases, stable in a narrow compositional and temperature range.

ASSOCIATED CONTENT

Supporting Information

The Supporting Information is available free of charge on the ACS Publications website at DOI: [10.1021/acs.chemmater.9b02239](https://doi.org/10.1021/acs.chemmater.9b02239).

Additional tables with interatomic distances, Rietveld refinement plots, and tables with parameters of XRD data collection and refinement (PDF)

Single crystal $\text{HT-Na}_{1-x}\text{Zn}_{4-y}\text{Sb}_3$ crystallographic information (CIF)

NaZn₄Sb₃ powder crystallographic information ([CIF](#))

AUTHOR INFORMATION

Corresponding Author

*(J.V.Z.) E-mail: yzaikina@iastate.edu.

ORCID

Bryan Owens-Baird: [0000-0003-3128-5363](https://orcid.org/0000-0003-3128-5363)

Yang Sun: [0000-0002-4344-2920](https://orcid.org/0000-0002-4344-2920)

Cai-Zhuang Wang: [0000-0002-0269-4785](https://orcid.org/0000-0002-0269-4785)

Julia V. Zaikina: [0000-0002-8755-1926](https://orcid.org/0000-0002-8755-1926)

Funding

The financial support for J.V.Z. startup funds from Iowa State University is gratefully acknowledged. The work at Ames Laboratory was supported by the U.S. Department of Energy (DOE), Office of Science, Basic Energy Sciences, Materials Science and Engineering Division, under Contract No. DE-AC02-07CH11358, including a grant of computer time at the National Energy Research Scientific Computing Center (NERSC) in Berkeley, CA. Use of the Advanced Photon Source at Argonne National Laboratory was supported by the U.S. Department of Energy, Office of Science, Office of Basic Energy Sciences, under Contract No. DE-AC02-06CH11357.

Notes

The authors declare no competing financial interest.

ACKNOWLEDGMENTS

We thank Dr. Arkady Ellern (Department of Chemistry, Iowa State University) for the help with SC XRD data collection, Dr. Kirill Kovnir (Department of Chemistry, Iowa State University, and US-DOE Ames Laboratory) for the access to DSC-TG and PPMS, and Warren Straszheim (Materials Analysis Research Laboratory, Iowa State University) for the help with SEM/EDXS measurement. Dr. Wenqian Xu and Dr. Andrey Yakovenko at 17-BM beamline, APS ANL, are acknowledged for help with high-temperature synchrotron powder XRD data collection.

REFERENCES

- (1) Gautier, R.; Zhang, X.; Hu, L.; Yu, L.; Lin, Y.; Sunde, T. O. L.; Chon, D.; Poepelmeier, K. R.; Zunger, A. Prediction and accelerated laboratory discovery of previously unknown 18-electron ABX compounds. *Nat. Chem.* **2015**, *7*, 308–316.
- (2) Curtarolo, S.; Hart, G. L. W.; Nardelli, M. B.; Mingo, N.; Sanvito, S.; Levy, O. The high-throughput highway to computational materials design. *Nat. Mater.* **2013**, *12*, 191–201.
- (3) Haynes, A. S.; Stoumpos, C. C.; Chen, H.; Chica, D.; Kanatzidis, M. G. Panoramic Synthesis as an Effective Materials Discovery Tool: The System Cs/Sn/P/Se as a Test Case. *J. Am. Chem. Soc.* **2017**, *139*, 10814–10821.
- (4) Jansen, M. Conceptual Inorganic Materials Discovery – A Road Map. *Adv. Mater.* **2015**, *27*, 3229–3242.
- (5) Alberi, K.; et al. The 2019 materials by design roadmap. *J. Phys. D: Appl. Phys.* **2019**, *52*, 013001.
- (6) Oliynyk, A. O.; Antono, E.; Sparks, T. D.; Ghadbeigi, L.; Gaultois, M. W.; Meredig, B.; Mar, A. High-Throughput Machine-Learning-Driven Synthesis of Full-Heusler Compounds. *Chem. Mater.* **2016**, *28*, 7324–7331.
- (7) Gvozdetskyi, V.; Bhaskar, G.; Batuk, M.; Zhao, X.; Wang, R.; Carnahan, S. L.; Hanrahan, M. P.; Ribeiro, R. A.; Canfield, P. C.; Rossini, A. J.; Wang, C.-Z.; Ho, K.-M.; Hadermann, J.; Zaikina, J. V. Computationally-driven discovery of a family of layered LiNiB polymorphs. *Angew. Chem., Int. Ed.* **2019**, DOI: [10.1002/anie.201907499](https://doi.org/10.1002/anie.201907499).
- (8) Shoemaker, D. P.; Hu, Y. J.; Chung, D. Y.; Halder, G. J.; Chupas, P. J.; Soderholm, L.; Mitchell, J. F.; Kanatzidis, M. G. In situ studies of a platform for metastable inorganic crystal growth and materials discovery. *Proc. Natl. Acad. Sci. U. S. A.* **2014**, *111*, 10922–10927.
- (9) Kanatzidis, M. G. Discovery-Synthesis, Design, and Prediction of Chalcogenide Phases. *Inorg. Chem.* **2017**, *56*, 3158–3173.
- (10) Cheong, S.; Watt, J.; Ingham, B.; Toney, M. F.; Tilley, R. D. In situ and ex situ studies of platinum nanocrystals: growth and evolution in solution. *J. Am. Chem. Soc.* **2009**, *131*, 14590–14595.
- (11) Bai, J.; Hong, J.; Chen, H.; Graetz, J.; Wang, F. Solvothermal synthesis of LiMn_{1-x}Fe_xPO₄ cathode materials: a study of reaction mechanisms by time-resolved in situ synchrotron X-ray diffraction. *J. Phys. Chem. C* **2015**, *119*, 2266–2276.
- (12) Jensen, K. M. O.; Tyrsted, C.; Bremholm, M.; Iversen, B. B. In situ studies of solvothermal synthesis of energy materials. *ChemSusChem* **2014**, *7*, 1594–1611.
- (13) Woo, K. E.; Wang, J.; Wu, K.; Lee, K.; Dolyniuk, J.-A.; Pan, S.; Kovnir, K. Mg-Si-As: An Unexplored System with Promising Nonlinear Optical Properties. *Adv. Funct. Mater.* **2018**, *28*, 1801589.
- (14) Owens-Baird, B.; Lee, S.; Kovnir, K. Two-dimensional metal NaCu_{6.3}Sb₃ and solid-state transformations of sodium copper antimonides. *Dalton Trans.* **2017**, *46*, 12438.
- (15) Hudak, B. M.; Depner, S. W.; Waetzig, G. R.; Talapatra, A.; Arroyave, R.; Banerjee, S.; Guiton, B. S. Real-time atomistic observation of structural phase transformations in individual hafnia nanorods. *Nat. Commun.* **2017**, *8*, 15316.
- (16) Ma, T.; Wang, S.; Chen, M.; Maligal-Ganesh, R. V.; Wang, L.-L.; Johnson, D. D.; Kramer, M. J.; Huang, W.; Zhou, L. Toward Phase and Catalysis Control: Tracking the Formation of Intermetallic Nanoparticles at Atomic Scale. *Chem.* **2019**, *5*, 1235–1247.
- (17) Vasquez, G.; Huq, A.; Lattner, S. E. In Situ Neutron Diffraction Studies of the Metal Flux Growth of Ba/Yb/Mg/Si Intermetallics. *Inorg. Chem.* **2019**, *58*, 8111–8119.
- (18) Schmidt, J.; Schnelle, W.; Grin, Y.; Kniep, R. Pulse plasma synthesis and chemical bonding in magnesium diboride. *Solid State Sci.* **2003**, *5*, 535–539.
- (19) Gvozdetskyi, V.; Hanrahan, M. P.; Ribeiro, R. A.; Kim, T.; Zhou, L.; Rossini, A. J.; Canfield, P. C.; Zaikina, J. V. Hydride route to alkali metal borides: a case study of lithium nickel borides. *Chem. - Eur. J.* **2019**, *25*, 4123–4135.
- (20) Cox, T.; Gvozdetskyi, V.; Owens-Baird, B.; Zaikina, J. V. Rapid phase screening via hydride route: a discovery of K_{8-x}Zn_{18+3x}Sb₁₆. *Chem. Mater.* **2018**, *30*, 8707–8715.
- (21) Gvozdetskyi, V.; Owens-Baird, B.; Hong, S.; Zaikina, J. V. Thermal stability and thermoelectric properties of NaZnSb. *Materials* **2019**, *12*, 48–62.
- (22) Zaikina, J. V.; Batuk, M.; Abakumov, A. M.; Navrotsky, A.; Kauzlarich, S. M. Facile Synthesis of Ba_{1-x}K_xFe₂As₂ Superconductors via Hydride Route. *J. Am. Chem. Soc.* **2014**, *136*, 16932–16939.
- (23) Zaikina, J. V.; Kwong, M. Y.; Baccam, B.; Kauzlarich, S. M. Superconductor-in-an-hour: Spark Plasma synthesis of Co and Ni-doped BaFe₂As₂. *Chem. Mater.* **2018**, *30*, 8883–8890.
- (24) Ma, X.; Xu, F.; Atkins, T. M.; Goforth, A. M.; Neiner, D.; Navrotsky, A.; Kauzlarich, S. M. A versatile low temperature synthetic route to Zintl phase precursors: Na₄Si₄, Na₄Ge₄ and K₄Ge₄ as examples. *Dalton Trans.* **2009**, *0*, 10250–10255.
- (25) Yi, T.; Chen, S.; Li, S.; Yang, H.; Bux, S.; Bian, Z.; Katcho, N. A.; Shakouri, A.; Mingo, N.; Fleurial, J. P.; Browning, N. D.; Kauzlarich, S. M. Synthesis and characterization of Mg₂Si/Si nanocomposites prepared from MgH₂ and silicon, and their thermoelectric properties. *J. Mater. Chem.* **2012**, *22*, 24805–24813.
- (26) Janka, O.; Zaikina, J. V.; Bux, S. K.; Tabatabaifar, H.; Yang, H.; Browning, N. D.; Kauzlarich, S. M. Microstructure investigations of Yb- and Bi-doped Mg₂Si prepared from metal hydrides for thermoelectric applications. *J. Solid State Chem.* **2017**, *245*, 152–159.
- (27) Sui, F.; Kauzlarich, S. M. Tuning Thermoelectric Properties of Type I Clathrate K_{8-x}Ba_xAl_{8+x}Si_{38-x} through Barium Substitution. *Chem. Mater.* **2016**, *28*, 3099–3107.

- (28) Perez, C. J.; Bates, V. J.; Kauzlarich, S. M. Hydride Synthesis and Thermoelectric Properties of Type-I Clathrate $K_8E_8Ge_{38}$ ($E = Al, Ga, In$). *Inorg. Chem.* **2019**, *58*, 1442–1450.
- (29) Kauzlarich, S. M. *Chemistry, structure, and bonding of Zintl phases and ions*; VCH Publishers Inc.: New York, U.S.A., 1996.
- (30) Fässler, T. F. *Zintl phases: principles and recent developments*; Book Series: Structure and Bonding; Springer-Verlag Berlin: Heidelberg, Germany, 2011; p 139.
- (31) Kauzlarich, S. M.; Zevalkink, A.; Toberer, E.; Snyder, G. J. Zintl phases: recent developments in thermoelectrics and future outlook. In *Thermoelectric materials and devices*; Nandhakumar, I., White, M. M., Beeby, S., Eds.; Book Series: RSC Energy and Environment Series; The Royal Society of Chemistry: London, United Kingdom, 2017; Vol. 17, pp 1–26.
- (32) Kazem, N.; Kauzlarich, M. Thermoelectric properties of Zintl antimonides. In *Handbook on the physics and chemistry of rare earth*; Bünzli, J.-C. G.; Pecharsky, V. K. North Holland: Amsterdam, The Netherlands, 2016; Vol. 50, pp 177–208.
- (33) Toberer, E. S.; May, A. F.; Snyder, G. J. Zintl chemistry for designing high efficiency thermoelectric materials. *Chem. Mater.* **2010**, *22*, 624–634.
- (34) Gascoin, F.; Ottensmann, S.; Stark, D.; Haile, S. M.; Snyder, G. J. Zintl phases as thermoelectric materials: Tuned transport properties of the compounds $Ca_xYb_{1-x}Zn_2Sb_2$. *Adv. Funct. Mater.* **2005**, *15*, 1860–1864.
- (35) Toberer, E. S.; May, A. F.; Melot, B. C.; Flage-Larsen, E.; Snyder, G. J. Electronic structure and transport in thermoelectric compounds AZn_2Sb_2 ($A = Sr, Ca, Yb, Eu$). *Dalton Trans.* **2010**, *39*, 1046–1054.
- (36) Brown, S. R.; Kauzlarich, S. M.; Gascoin, F.; Snyder, G. J. $Yb_{14}MnSb_{11}$: New high efficiency thermoelectric material for power generation. *Chem. Mater.* **2006**, *18*, 1873–1877.
- (37) Hu, Y.; Cerretti, G.; Kunz Wille, E. L.; Bux, S. K.; Kauzlarich, S. M. The remarkable crystal chemistry of the $Ca_{14}AlSb_{11}$ structure type, magnetic and thermoelectric properties. *J. Solid State Chem.* **2019**, *271*, 88–102.
- (38) *PDXL: Integrated X-ray powder diffraction software*, Version 2.8.1.1; Rigaku: 2018.
- (39) *Apex3*, Version 2017.3; Bruker: 2017.
- (40) Sheldrick, G. M. A short history of SHELX. *Acta Crystallogr., Sect. A: Found. Crystallogr.* **2008**, *A64*, 112–122.
- (41) Spek, A. L. Structure validation in chemical crystallography. *Acta Crystallogr., Sect. D: Biol. Crystallogr.* **2009**, *D65*, 148–155.
- (42) Boyle, P. D. COSET: a program for deriving and testing merohedral and pseudo-merohedral twin laws. *J. Appl. Crystallogr.* **2014**, *47*, 467–470.
- (43) Chupas, P. J.; Chapman, K. W.; Kurtz, C.; Hanson, J. C.; Lee, P. L.; Grey, C. P. A versatile sample-environment cell for non-ambient X-ray scattering experiments. *J. Appl. Crystallogr.* **2008**, *41*, 822–824.
- (44) Toby, B. H.; Von Dreele, R. B. GSAS-II: the genesis of a modern open-source all purpose crystallography software package. *J. Appl. Crystallogr.* **2013**, *46*, 544–549.
- (45) Kresse, G.; Furthmüller, J. Efficiency of ab-initio total energy calculations for metals and semiconductors using a plane-wave basis set. *Comput. Mater. Sci.* **1996**, *6*, 15–50.
- (46) Kresse, G.; Furthmüller, J. Efficient iterative schemes for ab initio total-energy calculations using a plane-wave basis set. *Phys. Rev. B: Condens. Matter Mater. Phys.* **1996**, *54*, 11169–11186.
- (47) Kresse, G.; Joubert, D. From ultrasoft pseudopotentials to the projector augmented-wave method. *Phys. Rev. B: Condens. Matter Mater. Phys.* **1999**, *59*, 1758–1775.
- (48) Blochl, P. E. Projector augmented-wave method. *Phys. Rev. B: Condens. Matter Mater. Phys.* **1994**, *50*, 17953–17979.
- (49) Perdew, J. P.; Burke, K.; Ernzerhof, M. Generalized Gradient Approximation Made Simple. *Phys. Rev. Lett.* **1996**, *77*, 3865–3868.
- (50) Kahlert, H.; Schuster, H. U. Ternary phases of sodium or potassium with elements of 2B-group and 5B-group. *Z. Naturforsch., B: J. Chem. Sci.* **1976**, *31*, 1538–1539.
- (51) Savelsberg, G.; Schaefer, H. On Ternary Pnictides and Chalkogenides of Alkaline Metals and IB- resp. II B-Elements (in German). *Z. Naturforsch., B: J. Chem. Sci.* **1978**, *33*, 370–373.
- (52) Snyder, G. J.; Christensen, M.; Nishibori, E.; Caillat, T.; Iversen, B. B. Disordered zinc in Zn_4Sb_3 with phonon-glass and electron-crystal thermoelectric properties. *Nat. Mater.* **2004**, *3*, 458–463.
- (53) Nylen, J.; Andersson, M.; Lidin, S.; Häussermann, U. The Structure of α - Zn_4Sb_3 : Ordering of the Phonon-Glass Thermoelectric Material β - Zn_4Sb_3 . *J. Am. Chem. Soc.* **2004**, *126* (50), 16306–16307.
- (54) Mozharivskyj, Y.; Janssen, Y.; Harringa, J. L.; Kracher, A.; Tsokol, A. O.; Miller, G. J. $Zn_{13}Sb_{10}$: A Structural and Landau Theoretical Analysis of Its Phase Transitions. *Chem. Mater.* **2006**, *18*, 822–831.
- (55) Nylen, J.; Lidin, S.; Andersson, M.; Iversen, B. B.; Newman, N.; Häussermann, U. Low-Temperature Structural Transitions in the Phonon-Glass Thermoelectric Material β - Zn_4Sb_3 : Ordering of Zn Interstitials and Defects. *Chem. Mater.* **2007**, *19*, 834–838.
- (56) Lo, C. W. T.; Svitlyk, V.; Chernyshov, D.; Mozharivskyj, Y. The updated Zn–Sb phase diagram. How to make pure $Zn_{13}Sb_{10}$ (“ Zn_4Sb_3 ”). *Dalton Trans.* **2018**, *47*, 11512–11520.
- (57) ICSD – the Inorganic Crystal Structure Database, FIZ – Karlsruhe, 2018.
- (58) Schroeder, G.; Schuster, H. U. LiZnSb, an additional ternary phase with a Wurzite-type lattice (in German). *Z. Naturforsch., B: J. Chem. Sci.* **1975**, *30*, 978–979.
- (59) He, H.; Stoyko, S. S.; Mar, A.; Bobev, S. Ternary $K_2Zn_5As_4$ -type pnictides $Rb_2Cd_5As_4$ and $Rb_2Zn_5Sb_4$, and the solid solution $Rb_2Cd_5(As,Sb)_4$. *Acta Crystallogr., Sect. C: Cryst. Struct. Commun.* **2013**, *69*, 455–459.
- (60) Carter, F. L.; Mazelsky, R. The ZnSb structure; A further enquiry. *J. Phys. Chem. Solids* **1964**, *25*, 571–581.
- (61) Wang, J.; Kovnir, K. Elusive β - Zn_8Sb_7 : A New Zinc Antimonide Thermoelectric. *J. Am. Chem. Soc.* **2015**, *137* (39), 12474–12477.
- (62) He, H.; Tyson, C.; Bobev, S. Eight-Coordinated Arsenic in the Zintl Phases $RbCd_4As_3$ and $RbZn_4As_3$: Synthesis and Structural Characterization. *Inorg. Chem.* **2011**, *50*, 8375–8383.
- (63) Cordier, G.; Ochmann, H. Crystal structure of trisodium tectodiantimonidoindate, Na_3InSb_2 . *Zeitschrift für Kristallographie* **1991**, *195*, 107–108.
- (64) Cordier, G.; Ochmann, H.; Schaefer, H. $Na_2Al_2Sb_3$ und $K_2Al_2Sb_3$, zwei neue Zintlphasen mit Schichtanionen. *Revue de Chimie Minérale* **1984**, *21*, 282–291.
- (65) Eisenmann, B.; Klein, J. Na_3SnSb_3 and K_3SnSb_4 , zwei neue Zintlphasen mit tetraedrischen SnSb₄-Baueinheiten. *Z. Naturforsch., B: J. Chem. Sci.* **1988**, *43*, 1156–1160.
- (66) Carrillo Cabrera, W.; Caroca Canales, N.; Von Schnering, H. G. Dipotassium Sodium Diantimonidoindate, $K_2Na[InSb_2]$, a compound with the polyanion $\infty^2[In_2Sb_2Sb_{4/2}]^{6-}$. *Z. Anorg. Allg. Chem.* **1993**, *619*, 1717–1720.
- (67) Saparov, B.; Saito, M.; Bobev, S. Syntheses, and crystal and electronic structures of the new Zintl phases Na_2ACdSb_2 and K_2ACdSb_2 ($A = Ca, Sr, Ba, Eu, Yb$): Structural relationship with Yb_2CdSb_2 and the solid solutions $Sr_{2-x}A_xCdSb_2$, $Ba_{2-x}A_xCdSb_2$ and $Eu_{2-x}Yb_xCdSb_2$. *J. Solid State Chem.* **2011**, *184*, 432–440.
- (68) Kim, H. S.; Gibbs, Z. M.; Tang, Y.; Wang, H.; Snyder, G. J. Characterization of Lorenz number with Seebeck coefficient measurement. *APL Mater.* **2015**, *3*, 041506–041511.
- (69) Stefanoski, S.; Beekman, M.; Nolas, G. S. Inorganic Clathrates for Thermoelectric Applications. In *The Physics and Chemistry of Inorganic Clathrates*; Springer Series in Materials Science; Nolas, G., Ed.; Springer: Dordrecht, 2014; Vol 199, Ch. 6, pp 169–191.
- (70) Cohn, J. L.; Nolas, G. S.; Fessatidis, V.; Metcalf, T. H.; Slack, G. A. Glasslike Heat Conduction in High-Mobility Crystalline Semiconductors. *Phys. Rev. Lett.* **1999**, *82*, 779–782.